

POLITECNICO DI TORINO

Corso di Laurea Magistrale in Ingegneria Biomedica

Tesi di Laurea Magistrale

Evaluating Stretchability of Metals on PDMS: The Impact of Deposition Techniques and Temperature



**Politecnico
di Torino**

Relatore:
Danilo Demarchi

Candidato:
Chiara Antonini

Anno Accademico 2023/2024

Summary

This study investigates the stretchability of conductive thin films on flexible substrates, focusing on the influence of temperature as a key microfabrication parameter. Stretching tests were performed on gold and platinum samples to assess their mechanical properties based on the deposition techniques used. This study explores test tracks produced through sputtering deposition and thermal evaporation. The results suggest that sputtered gold samples demonstrate superior mechanical characteristics compared to those obtained via thermal evaporation, indicating potential advantages for flexible electronic implants. Furthermore, the study examines the impact of temperature on mechanical performances in terms of the stretchability of the platinum deposition as well, underscoring its significant influence on device performance. While the tests are not exhaustive, they lay the groundwork and offer insights for future investigations in the design of neurological and biomedical devices. This study contributes to understanding the intricate relationships between temperature and mechanical behaviour in flexible implantable electronics, paving the way for future developments in neurological therapies and biomedical engineering.

Table of contents

Summary	1
1 Introduction	5
1.1 Aim Of The Study	9
2.2 State Of The Art.....	10
2 Background.....	15
2.1 Thin Films	15
2.1.1 Adhesion Layers	16
2.2 Physical Vapor Deposition.....	17
2.2.1 Thermal Evaporation Deposition	17
2.2.2 Sputtering Deposition	19
2.3 Scanning Electron Microscopy.....	21
2.4 Spin Coating.....	22
2.5 Polymers	23
2.6 Metals	27
2.6.1 Gold.....	27
2.6.2 Platinum.....	27
3 Methods	28
3.1 Microfabrication	28
3.1.1 Glass Wafer Plasma Activation	29
3.2.2 PSS Spin Coating.....	30
3.3.3 PDMS Preparation And PDMS Spin Coating	30
3.3.4 PET Lamination.....	32
3.3.5 Mask Design And Laser Cutting	33
3.3.6 Detachment From The Glass Substrate	38

3.3.7 Peeling Off The Cut PET Mask	39
3.3.8 Deposition	40
3.3.9 Peeling Off The PET Mask	43
3.2 Encapsulation and interconnections.....	44
3.2.1 Silver Paste Application	45
3.2.2 Silicone Application	46
3.3.3 PDMS Coating	47
3.3 Samples Characterization.....	49
3.3.1 Optical Microscopy And SEM Analysis	49
3.3.2 Four Probes Resistance Measurements.....	50
3.4 Mechanical Stretch Testing.....	51
3.5 Depositions	53
4. Results.....	56
4.1 Optical Microscopy	56
4.1.1 CrAu_S_R	56
4.1.2 CrAu_S_70	57
4.1.3 CrAu_T	58
4.1.4 TiPt_S_RT	59
4.1.5 TiPt_S_50	60
4.1.6 TiPt_S_70	61
4.2 Four Probes Resistance Measurements.....	62
4.3 SEM Analysis.....	64
4.3.1 CrAu_S_RT	65
4.3.2 CrAu_S_70	66
4.3.3 CrAu_T	67
4.3.4 TiPt_S_RT	68
4.3.5 TiPt_S_50	69
4.3.6 TiPt_S_70	70
4.4 Mechanical Testing	71

5 Discussion.....	76
6 Conclusion	84
References/bibliography	86

1 Introduction

Over the past few years, the microelectronics industry has been facing the challenge of keeping up with the ever-evolving requirements in the field of medicine. The integration of electrical signals has emerged as a critical component for a wide range of new medical monitoring and therapy techniques developed in the last decade. From monitoring vital signs to providing targeted therapy, the role of microelectronics in modern medicine cannot be overstated. The area of implantable electronics, which involves the use of various electronic devices to interact with specific targets within the body for purposes such as recording, stimulation, sensing, and aiding tissue regeneration, has been extensively studied [1], [2], [3], [4], [5]. With the ability to bend and fold, these electronics offer versatility and adaptability to the complex architecture of the human body, far surpassing traditional electronics.

Flexible electronics technology has shown great potential in neurological applications: one of its most significant applications is in recording biological signals generated by the body's nervous system. This technology enables researchers to monitor the electrical activity of the brain and other body parts in real time, helping them better understand the underlying mechanisms of neurological disorders. Moreover, flexible and stretchable electronic technology has also paved the way for electrical stimulation of the nervous system, which is an effective treatment for various pathologies, such as chronic pain, epilepsy, Parkinson's disease [6] Chron's disease [7], and other movement disorders. By stimulating specific areas of the brain, researchers can alleviate symptoms associated with these conditions, improving the quality of life of patients. For example, cochlear implants [8], Utah array [9], deep brain stimulators [6], and cardiac pacemakers [10] are representative developments of implantable devices for therapeutic application. Medical electronics, while offering significant potential, present substantial challenges as well.

One of these challenges is developing sophisticated devices and materials that can effectively and seamlessly integrate with the human body while performing their intended function. Flexible and stretchable electronics aim to minimize mechanical discrepancies when interfacing with biological tissues, particularly soft neural tissue. This is a crucial approach in neuroengineering history and in addressing current challenges in neuroscience. Unlike rigid electronics, flexible and stretchable

electronics utilize materials with lower Young's modulus, increasing mechanical compliance and aligning more closely with the mechanical properties of the interfaced neural tissue [11], [12]. Overall, the use of flexible micro-electronic technology in neurological applications can revolutionize medicine and significantly improve our understanding and treatment of various neurological disorders.

Developing stretchable implantable electronics is a complex and challenging task that requires careful material selection capable of withstanding repeated stretching and contraction cycles without compromising biocompatibility, as well as mechanical and electrical properties. Integration of various materials and technologies is essential to ensure robust mechanical strength, superior electronic performance, and essential attributes for flexible, stretchable implantable devices. These attributes may encompass mechanical flexibility, and surface characteristics such as wettability, permeability, biocompatibility, bioresorbability, thermal stability, surface smoothness, and minimal thickness [13]. In sensing applications, the flexibility and stretchability of materials are critical. Polymers are especially useful in this context because of the reversible nature of their polymeric backbones.

One of the primary concerns in this area is exploring technologies that simultaneously provide functional devices and reproducible fabrication protocols. The advancement of flexible and stretchable electronics requires sophisticated technologies and manufacturing methods capable of adapting to the distinctive properties of these materials.

The following research focuses, as its main application, on cuff implantable electrodes designed for peripheral nerves, which are areas that experience constant mechanical stress. Nerve tissues endure continuous movement and pressure, which can cause the electrodes to develop cracks. If these cracks become too large, the conductor's resistance increases dramatically, eventually becoming nonconductive anymore. This makes the conductor incapable of transmitting electrical signals, thus compromising the device's functionality. Stretchable electrodes have the potential to enhance the performance of neural implants by addressing issues related to tissue swelling and mechanical stress following implantation. The stretchability of these electrodes is essential for safe handling during medical procedures, allowing them to be wrapped around nerves and securely clamped without the risk of damage.

Implantable electrodes are usually made of metals like platinum and gold and are fabricated on flexible substrates to adapt to the pliable nature of human tissues. Modern implantable electrodes are made to be flexible to accommodate the continuous movements of nervous tissue. However, a common issue after implantation is the body's response, often resulting in the buildup of fibrous tissue around the electrode. This tissue, mainly composed of collagen, forms a scar tissue barrier that hinders direct interaction between the electrode and the surrounding tissues, often leading to the formation of a fibrous capsule around the electrode. In this case, the crucial property that maintains the device's performance is its stretchability.

Flexibility and stretchability are often misunderstood but refer to different characteristics of materials. Flexibility describes how easily a material can bend or twist without breaking, indicating how well it can conform to various shapes, crucial for applications needing adaptability to different forms. Stretchability refers to a material's ability to elongate under tension, important for materials that need to expand significantly without losing their structural integrity. For example, a material like a flexible wire can bend readily, whereas a stretchable fabric like elastane can be stretched considerably.

The innovation of this project is specifically the analysis of the stretchability of these devices, which is crucial given that, as previously described, inflammation of the tissue can compromise the effectiveness of the device over its entire lifecycle. Biochemical sensors rely on parameters such as the electrode's resistance and capacitance to measure specific parameters. During implantation, the electrode is placed on relaxed tissue at its original dimensions. However, as mentioned earlier, in the event of inflammation—a common occurrence in these cases—the tissue expands, pulling the electrode along with it. If the electrode's design and fabrication parameters are not optimized for tensile resistance, this stretching force could cause cracks to form on the surface of the electrode. In the best-case scenario, these cracks would increase the electrode's resistance and decrease its capacitance, undermining signal stability and sensitivity. In the worst-case scenario, the cracks could render the electrode non-conductive altogether.

This thesis contributes to the NerveRepack project, an ambitious initiative involving numerous international partners, including the University Politecnico di Torino. The

main goal of NerveRepack is to develop a new generation of bidirectional implantable electrodes designed to connect the human nervous system with external mechatronic devices such as exoskeletons and prosthetic exoskeletons. This project aims to provide significant support to individuals with limb amputations or lower limb paralysis, enabling the recovery of motor and sensory functions.

In this context, I have worked with the team at the University of South-Eastern Norway, focusing on the design of the implantable electrodes.

The thesis begins with an introductory paragraph, followed by an explanation of the project's objectives and an overview of thin films, deposition techniques, and materials used as preliminary theory. This is followed by a review of relevant literature. The methods section outlines the microfabrication and encapsulation processes used for the samples and concludes with a description of the analyses conducted, including optical microscopy, SEM microscopy, assessment of track resistance, and mechanical tests. The results are then presented, focusing on the optical microscopy images and SEM analysis for each type of sample, as well as the mechanical test results and analysis of the challenges encountered during the project.

1.1 Aim Of The Study

The objective of this study is to investigate the electrical and mechanical properties of conductive metallic thin films when deposited on a flexible substrate. Previous research has indicated that standalone thin metal films are susceptible to breaking when subjected to tensile strain of approximately 1% [14]. Applying a thin metal layer to a flexible substrate has been found to enhance the mechanical and electrical performance of conductors under mechanical stress. Various factors, including the chemical and physical properties of the conductive material, the polymer substrate, and the deposition technique, play a role in this process. This project aims to assess the impact of some of these factors on the stretchability of the metallization. During the project, different deposition techniques have been employed and various materials have been subjected to testing.

We created testing tracks through microfabrication using our research group's optimized microfabrication process. The standard protocol involved depositing gold tracks using the thermal evaporation technique as per our colleagues' method. The thermal evaporation samples served to generate control samples. These control samples were subsequently compared to those fabricated using sputtering deposition at varying temperatures to evaluate the difference in their stretchability. Both gold and platinum were explored as candidate materials for the electrodes; however, research on platinum underscores that it remains the material of choice for creating implantable neural electrodes due to its superior electrochemical stability and biocompatibility [15].

After applying the conductive layers, we examined its structure using optical microscopy and SEM. Subsequently, we performed resistance measurements while subjecting the sample to tensile stress testing to assess changes in its electrical behaviour. While existing literature on stretchability primarily focuses on gold electrodes manufactured through thermal deposition, this study aims to evaluate the stretching properties of electrodes produced using sputtering with different temperatures.

2.2 State Of The Art

Before starting the testing design, I conducted a literature review using the Scopus database with the keywords "thin," "stretchable," "metal," and "films," which yielded 318 results. A second query using the keywords "electrodes," "gold," and "deposition" resulted in 5,525 papers. Articles published before the year 2000 were excluded in order to ensure that the techniques and methodologies adopted are aligned with the most recent advancements in the field. The analyzed articles share a common focus on deposition using physical vapour deposition techniques on a polymeric substrate. Additionally, when discussing gold deposition in articles, I examined the methods to determine the various protocols for microfabricating the samples and evaluating their stretchability. We found that thermal evaporation is the common method of choice for fabricating thin stretchable gold films on PDMS. Since the 2000s, numerous groups have been working on developing electrodes on flexible substrates. Most research teams have opted to use platinum and gold as the preferred metals for synthesizing these electrodes, with PDMS as the substrate.

“Several methods have been reported for depositing metal films on flexible substrates, including physical vapour deposition (PVD), direct transfer of metal precursors or metal nanoparticles onto polymer substrates, electroless deposition (ELD), and electroplating [16]”.

According to the literature research, the ability of a thin metallic layer on a flexible substrate to stretch is primarily influenced by two distinct mechanisms: the formation of wrinkles on the surface and the existence of microcracks.

Lacour et al. [17], in 2003, developed gold electrodes on an elastomeric substrate with membranes of polydimethylsiloxane (PDMS). They deposited a 5 nm thick layer of chromium and a 100 nm thick layer of gold in one run by successive electron beam evaporation onto elastomeric substrates of PDMS held at room temperature. The team found that a metal film on an elastomer substrate can be stretched far beyond the fracture strain of a freestanding metal film (which is typically just 1%), and still remain electrically conductive. Below 8% strain, the resistance increased proportionally with strain, accompanied by the appearance of small cracks at the edges. Beyond 8% strain, more extensive cracks developed across the width of the

stripe, leading to a significant rise in resistance. Remarkably, even at strains exceeding 15%, where substantial cracking occurred, the Au stripe remained electrically conductive. This was attributed to a thin conductive layer, possibly only one atom thick, remaining intact at the bottom of the cracks. Complete loss of electrical continuity was observed only at an external strain of 23%, where the resistance became infinite. The study concluded that inducing a surface wave pattern in gold stripes significantly enhances their stretchability.

By following the research conducted by Lacour et al.[17], Jones et al. [18], demonstrated that gold films on elastomers with built-in compressive stress can maintain conductivity up to 22% tensile strain by forming ordered waves when buckled. Key to the design of these stretchable interconnects is the initial buckled, wavy morphology of the metal film on the elastomeric substrate. The study claims that the stretchability depends on both the substrate's properties and the characteristics (amplitude and wavelength) of the wavy metal film.

A study by Sigurd Wagner et al. [14] underlines again how the stretchability of thin-film conductors on relaxed PDMS substrates depends significantly on wrinkling during the deposition of gold films on these substrates. Two distinct topographies were observed: buckled and flat films. Buckled films, exhibiting a wavy structure, maintained electrical continuity and could endure significant mechanical strain before failure. Flat films, characterized by a network of micro-cracks, displayed higher initial electrical resistance and less stretchability. The resistance of buckled samples increased linearly with strain until a critical point, beyond which the resistance rose sharply and the samples eventually failed. In contrast, flat samples exhibited a steady increase in resistance under strain due to the presence of micro-cracks. The study concludes that the built-in stress during deposition influences the formation of wrinkles, which in turn affects the mechanical and electrical performance of the films. Thus, controlling the wrinkling process is crucial for enhancing the stretchability of metal films on flexible substrates.

Graz et al. work [19], shows how gold thin-films of 50 nm thickness on silicone membranes demonstrated reversible stretchability and continuous electrical conduction up to 20% strain. The films develop interconnected islands through microcracks during cycling, maintaining stable electrical resistance over 250,000 cycles. The researchers state that these cracks allow the film to stretch and contract

without electrical failure, forming a network that adapts to mechanical strain. This crack-induced island structure supports the film's elasticity, showing a consistent electrical resistance profile even after extensive stretching, making it promising for flexible electronic applications.

A study conducted by Adrega, T et al. [20] in 2010 successfully developed stretchable gold conductors within polydimethylsiloxane (PDMS) films using standard photolithography. They have the ability to withstand both uni-axial (1D) and radial (2D) stretching with tens of percent strain, and their electrical response shows a nonlinear increase with strain that is reversible. The stretchability is achieved through a network of micro-cracks (~100 nm long) distributed within the metal film on PDMS. During stretching, micro-cracks elongate in both directions in 1D, while in 2D, they form islands, leaving the gold microstructure intact.

Juan Zhu and colleagues [21] developed a strain sensor utilizing a 50 nm thick layer of gold (Au) that was deposited directly onto either freshly prepared PDMS (F-PDMS) or plasma-treated PDMS (P-PDMS) through thermal evaporation. By adjusting the surface wettability of the elastomer substrate underneath a gold (Au) sensing layer, different crack morphologies (from cracked domains to cut-through cracks) in the Au layer were achieved. Cracked domains were found to significantly enhance stretchability, enabling strains over 100%, owing to their dense distribution. This tunability in crack morphology enabled precise control over sensor performance, facilitating applications across a spectrum of needs, from monitoring large-scale deformations to capturing subtle physiological signals.

Kim et al. study [22] introduces a method to produce highly stretchable and robust metal thin films using elastomeric substrates treated with thiol-containing silanes, exploiting the phenomenon of solvent eruption during metal thermal evaporation. The residual solvent content in the substrate influences the topography of radial nanocracks in the metal film, with an optimal range of 0.2–0.3 wt % for high-density radial nanocrack formation. These nanocracked gold films (NC-GF) exhibit excellent electrical characteristics, with only a moderate increase in electrical resistance under 100% strain and high stability during stretching cycles.

Yu and his team [23] investigated the spontaneous formation of localized wrinkling patterns around channel cracks in metal films deposited on soft polymer substrates.

The mechanism involves the initiation of channel cracks due to high tensile stress during the sputtering and annealing processes. Near the crack tips, irreversible plastic deformation of the film occurs, followed by the development of anisotropic compressive stress zones that induce ordered, straight wrinkles.

Chuan Fei Guo's team [24] in 2015 developed gold nanomeshes capable of conducting electricity, biocompatible, and entirely resistant to fatigue. The researchers achieved compressed Au nanomeshes by attaching free-floating Au nanomeshes onto a pre-stretched polydimethylsiloxane (PDMS) substrate, which they then dried with compressed airflow and slowly released the PDMS substrate. They conducted stretching cycling and one-time stretching/bending cycling at various strain rates. The team demonstrated innovative stretchable and transparent electrodes that offer possibilities for stretchable electronics and transducers. This study highlights the pre-strained Au nanomeshes on a smooth substrate that can undergo cyclic stretching to large strains (>100%) for over 50,000 cycles without experiencing any fatigue.

By enhancing the wrinkling of the surface of the deposition and the density of the microcracks, different researchers were able to apply these technologies to the biological signal recording field.

Zhang Fu-Tao and his research team [16] have developed flexible electrodes using electroless deposition. These electrodes are primarily made from metals such as copper, nickel, and silver. PDMS films underwent a thorough cleaning process with acetone, ethanol, and water before being treated with APTES solution and dopamine. Using this method, researchers successfully produced a flexible and stretchable Cu-PDMS conductor, demonstrating outstanding metallic conductivity of 1.2×10^7 S/m, even under the longest stretch strain of 700%.

The same approach used by Lacour in 2003 [17] has been used for fabricating soft neural electrodes as reported in [25],[26]. These electrodes were specifically designed for selective nerve stimulation in large animals. They are made of a stretchable silicone-based belt-like structure, which allows for seamless implantation around nerves of different sizes without causing excessive compression. Electrochemical assessments confirmed that the electrode has intimate contact with the nerves, ensuring stable performance in varied conditions. Preliminary

biocompatibility evaluations showed minimal nerve tissue growth and demyelination, indicating that the electrode is suitable for long-term implantation in large animal models.

2 Background

2.1 Thin Films

The fabrication of the testing tracks proposed in this work is based on the deposition of thin metal films. Commonly used conductive materials include gold, platinum, and titanium.

“In thin films, at least one material dimension is small, typically the thickness. For narrow lines, two dimensions are small, and for dots, all three dimensions are small. The thickness of the thin film results in surface effects such as surface scattering of electrons, leading to size-dependent resistivity. Additionally, the density of thin films is often much lower than that of bulk materials and the thin-film resistivity is always higher than that of the bulk material. Different deposition systems and materials can result in vastly different thin-film properties. For example, gold thin films have resistivity values similar to bulk metals, most other metals have resistivity values about twice as high as bulk metals” [27].

When deposited on wafers, thin films experience either compressive or tensile stresses. Two common types of these stresses are residual and intrinsic stresses. Residual stresses are caused by excessive thermal stresses induced in thin films due to the mismatch of the CTEs of the thin film material and substrate during deposition at high temperatures. This results in the previously flat surface of the metallic thin film becoming curved. Intrinsic stresses are induced by the reaggregation of crystalline grains of thin film material, typically occurring in physical deposition processes like sputtering at low temperatures [28].

In general, high-temperature depositions result in smoother films [27].

2.1.1 Adhesion Layers

Ensuring strong adhesion is a crucial consideration in thin-layer technology, with surface cleanliness being a key factor. Even the slightest residue or dirt left during pre-deposition steps can significantly impact the layer's ability to adhere to the substrate. Adhesion layers are frequently employed to enhance and improve adhesion.

The deposition technique can also impact adhesion. For example, sputtering can dislodge loosely bound atoms due to energetic ions and atoms, while evaporation doesn't inherently remove weakly bonded atoms [27].

For this particular project, two metals were used as adhesion layers: chromium was used as the adhesion layer between the thin gold film and the substrate, and titanium was used as the adhesion layer between the platinum film and the substrate.

When gold is deposited directly onto PDMS, adhesion can be limited because PDMS is a non-polarized surface and is relatively chemically inert. Chromium, being a reactive metal, can form chemical bonds with the surface functional groups of PDMS, thereby enhancing the anchoring of gold. When chromium is deposited on gold, it forms strong metallic bonds through the creation of a solid solution or alloy, ensuring a robust interface between the two metals. On the other hand, chromium adheres to PDMS through both chemical and physical interactions. Chemically, chromium reacts with the oxygen atoms in the PDMS surface to form silicate compounds or other surface interactions, establishing a durable bond. Physically, chromium adheres to the PDMS through van der Waals forces and mechanical interlocking due to the surface roughness and energy characteristics of PDMS.

Titanium is commonly used as an adhesion layer between platinum and PDMS due to its excellent adhesive properties and compatibility with both materials. Titanium forms a strong interfacial bond with platinum, which is crucial for ensuring good adhesion and preventing delamination during subsequent processing or use. Additionally, titanium's reactivity allows it to create a stable interface by forming a titanium-platinum alloy layer, which enhances the mechanical stability of the bond. Moreover, titanium provides a barrier that prevents diffusion between platinum and PDMS, which could otherwise degrade the bond quality over time.

The adhesion layers were deposited directly onto the substrate using commonly employed deposition techniques such as thermal deposition or sputtering, all performed in the same chamber as the conductive layer deposition. The adhesion layers employed had a thickness of 7 nm.

2.2 Physical Vapor Deposition

During the project, two physical vapor deposition (PVD) techniques were primarily utilized: thermal evaporation and sputtering. The following sections discuss the physical principles underlying these two deposition methods.

2.2.1 Thermal Evaporation Deposition

Thermal deposition relies on the key principle of metal evaporation. “Heated metals have high vapour pressures and in high vacuum, the evaporated atoms will be transported to the substrate” [27].

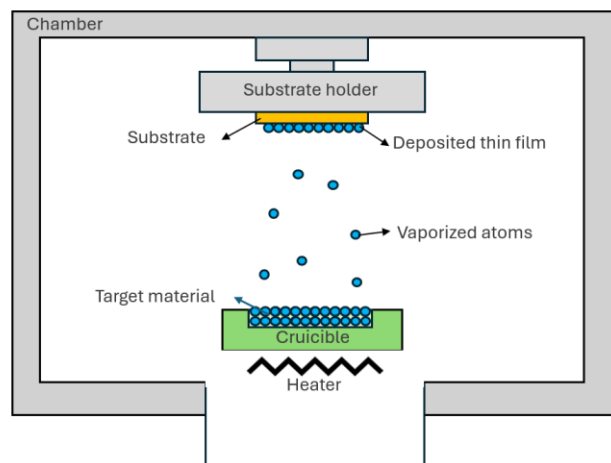


Figure 1- Schematic representation of thermal evaporation and the reaction chamber. At the top, the substrate holder supports the substrate. Blue circles represent the atoms of the thin film being deposited on the substrate and the vaporized atoms in transit. Below, the target material is contained within a crucible and heated by a heater.

The procedure requires a high vacuum chamber ranging from 10^6 - 10^{12} Torr. Achieving this level of vacuum necessitated several hours of preparation in our clean room. To reach a pressure of 10^6 Torr, approximately four to five hours were necessary. This procedure is time-consuming, not for the deposition process itself, which can take mere minutes depending on the deposition rate of the deposited metal, but for the creation of the vacuum, which is a much lengthier process.

To obtain the deposition, the desired material fragments are collected and placed into a crucible that can withstand higher temperatures than the metal to be deposited. The applied voltage causes the material to liquefy and evaporate, dispersing throughout the vacuum. The substrate is positioned face-down on top of the crucible to ensure that the entire wafer is coated evenly with the evaporated material. Generally, the deposition rate can vary from 0.1 to 20 Å/s with thermal evaporation. To improve the evenness of the layer that is being deposited, it is possible to rotate and tilt the substrate, altering its orientation and creating a more uniform thickness across the surface.

The thickness of the layer being deposited can be accurately determined using a crystal sensor that oscillates at a specific frequency within the chamber. As the crystal becomes coated with the deposited material, its mass changes, leading to a corresponding decrease in the frequency of oscillation. By monitoring this decrease in frequency, it is possible to gauge the thickness of both the metal deposited on the crystal and the substrate accurately. Thermal deposition is used commonly for metals such as Au, Ag, and Cr.

2.2.2 Sputtering Deposition

Sputtering is the most important PVD method, and it is generally used to deposit thin films on the order of 100 Å thick.

The following image represents a DC sputtering system, wherein the target holds the desired raw material for deposition onto the substrate. The target is negatively charged through a power source, while the substrate, the surface on which the deposition is to take place, is positively charged. The applied voltage ranges from 2 kV to 5 kV.

Then an inert gas, typically Argon, is introduced in the chamber. This combination of temperature, vacuum, and voltage results in the creation of plasma between the anode and cathode: the area is filled with a blend of ions, electrons, and other elements.

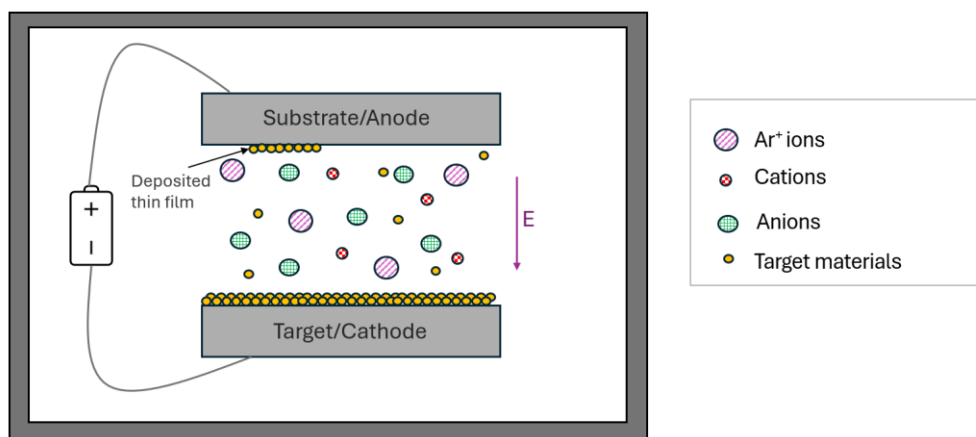


Figure 2- Schematic representation of a sputtering system and its reaction chamber. The diagram illustrates the substrate holder at the top with the substrate mounted. Violet arrows represent argon ions, green circles denote target atoms being sputtered, and red circles indicate secondary electrons. The target material is shown in orange and is bombarded by the accelerated argon ions, which are energized by a voltage generator.

The sputtering process is carried out with plasma under a very low pressure (in the study case, in high vacuum around 10^{-4} Pa) [28].

The accelerated Ar^+ ions penetrate the target, and upon impact, the raw material of the target is released. While the plasma electrons are also accelerated towards the substrate, their small size renders their impact negligible. In a sputtering process, the primary objective is to propel positively charged ions toward the cathode/target, which results in the disintegration of material and consequent release. The atoms ejected from the target will travel through the vacuum to reach the substrate wafers. “As they travel, these sputtered atoms undergo numerous collisions, a process known as thermalization. During thermalization, high-energy sputtered particles (equivalent to approximately 60,000 K for 5 eV) collide with cooler argon gas (at about 300 K), causing them to lose energy and cool down. This cooling process effectively decreases the energy of particles reaching the substrate, thereby reducing the particle flux and subsequently lowering the deposition rate” [27].

Figure 2 captures a shutter that serves as a physical barrier between the plasma zone and the target area. This is necessary to allow sufficient time for the creation of high-quality plasma. Once the plasma is prepared to strike the target, the shutter is released, and the plasma begins to accelerate toward the target, producing the desired effect.

Sputtering yield (Y) is the number of target atoms ejected per incident per incident ion. Refractory metals, such as chromium, exhibit low sputtering yields, leading to reduced deposition rates. This phenomenon can be attributed to their high resistivity and low thermal conductivity, which are inherent properties of refractory metals [27].

To summarize, the process of evaporation deposits atoms with low energy of around 0.1 eV, whereas sputtering deposits high energy atoms ranging from 1 eV to 10 eV. The significance of this is that sputtering usually produces better adhesion to the substrate surface when compared to evaporation. Evaporation requires higher vacuum conditions, which are highly directional and result in lower impurities. On the other hand, sputtering can be performed in lower vacuum conditions, which are less directional, as the plasma atoms are emitted from various directions. Furthermore, evaporation has a point source, which can lead to poor uniformity, whereas the parallel plate source of sputtering usually results in better uniformity. Additionally,

rotating the source during sputtering helps to overcome shadowing problems and ensure complete coverage [29].

2.3 Scanning Electron Microscopy

“Scanning Electron Microscopy (SEM) stands out as one of the most widely utilized types of electron microscopes, ideal for examining microscopic structures by scanning material surfaces. SEM achieves a minimum resolution down to 5 nm. An SEM image is generated by directing a focused electron beam across the specimen's surface. A key characteristic of SEM images is their three-dimensional appearance, enabled by the microscope's large depth of field [27].”

“The SEM apparatus includes an electron gun and a sequence of electromagnetic lenses and apertures. The electron gun emits a finely focused electron beam for surface scanning. The optical path in SEM passes through multiple electromagnetic lenses. Two types of electron signals are particularly valuable in SEM: backscattered electrons (BSEs) and secondary electrons (SEs). When high-energy electrons collide with a specimen, they undergo either elastic or inelastic scattering. Elastic scattering produces BSEs—electrons incident on atoms in the specimen that scatter back—while inelastic scattering produces SEs—electrons ejected from atoms in the specimen. SEs travel at wide deflection angles towards the detector, whereas BSEs travel directly towards it. Both SEs and BSEs resulting from scattering serve as signal sources for generating SEM images [27].”

“The resolution of SEM imaging depends on the cross-sectional diameter of the scanning probe. Therefore, the size of the probe limits the size of features that can be resolved on the specimen's surface. While reducing the probe size is necessary, it alone does not guarantee high-resolution SEM images. Achieving high-resolution images requires sufficient signal electrons for each pixel, crucial for distinguishing signals from background noise. The number of signal electrons is directly proportional to the number of incident electrons in the probe, implying that the probe current must exceed a minimum threshold to obtain adequate signal strength [30]” .

2.4 Spin Coating

Spin-coating is widely employed to achieve uniform and repeatable thin film coatings over large surfaces, ensuring precise structural consistency. This technique stands out due to its capability to uniformly apply thin films onto flat substrates up to a substantial diameter of 30 cm, ensuring highly controlled and repeatable film thickness [30].

“A typical spin process consists of a dispense step in which the resin fluid is deposited onto the substrate surface. The static dispense step is simply depositing a small puddle of fluid on or near the center of the substrate” [31]. “This can range from 1 to 10 cm³ depending on the viscosity of the fluid and the size of the substrate to be coated” [32].

The subsequent phase is referred to as the substrate acceleration phase. During this stage, the substrate undergoes rotation at a few revolutions per minute (rpm), utilizing centrifugal force to evenly spread a thin layer of resist across its surface. This method provides control over the deposited layer's thickness by adjusting the rotational speed and the volume of photoresist applied. This phase is typically characterized by the forceful expulsion of excess fluid from the wafer surface due to the rotational movement [33].

In the subsequent stage, the substrate continues to spin at a consistent rate, where the dominant forces are viscous forces governing the thinning behavior of the fluid. This process typically results in a uniform thinning of the fluid layer across the substrate surface [31]. “Therefore, factors such as surface tension, viscosity, rotational speed, and other variables can lead to slight variations in coating thickness along the edge of the wafer” [34].

As the preceding stage progresses, the thickness of the fluid layer reaches a state where viscosity effects result in minimal net fluid flow. At this juncture, the dominant process in the coating becomes the evaporation of any volatile solvent species [31]. Indeed, at this stage, the coating effectively undergoes a "gelation" process. As the volatile solvents are evaporated, the viscosity of the remaining solution increases, essentially locking the coating in place [33]. Spin coating is a quick and commonly used method that only requires a few seconds of rotation. However, it is not suitable

for non-rotation-symmetric substrates, such as triangular wafers or pieces of wafer, as it cannot deposit photoresist evenly on angled surfaces. By adjusting the speed rate, the thickness of the photoresist layer can be modulated.

2.5 Polymers

The thin layers of gold and platinum were deposited onto a flexible Polydimethylsiloxane substrate. A glass wafer served as a support, on which a layer of Polydimethylsiloxane was applied. To make it easier to remove the PDMS from the glass wafer, a layer of Polystyrene sulfonate was used. A Polyethylene terephthalate (PET) mask was used to create the deposition pattern.

Polymers are large molecules composed of repeating monomer units with molecular weights exceeding 1000 Daltons. Polymerization, facilitated by chemical reactions among these structural units, transforms monomers into polymers, resulting in either linear or cross-linked configurations based on the monomers' functional groups. These three-dimensional networks lack a distinct melting point but instead exhibit a softening range known as the melting interval. Polymers are categorized according to their thermal behavior. Thermoplastic polymers, like polyethylene and polystyrene, are typically linear or branched and can be melted and solidified upon cooling. Elastomers, such as polydimethylsiloxane, feature loose cross-linking that allows stretching and returning to their original shape. Conversely, thermosetting polymers are heavily cross-linked, rendering them brittle and rigid with minimal softening at high temperatures [35].

Polymers, including plastics and adhesives, have become increasingly important in microfabrication due to their numerous advantages, such as low cost of raw materials and production processes, lightweight, high corrosion resistance, high electric resistance, high flexibility in structures, high dimensional stability [28]. Polymeric materials possess the ability to be rendered inert to biomolecule interaction while allowing for uniform surface property modification. Biomedical applications are better served by polymers due to their affordability, chemical inertness, low electrical and

thermal conductivity, ease of surface modification, and compatibility with biological materials [35].

2.5.1 Polydimethylsiloxane

“Polydimethylsiloxane (PDMS) is a highly utilized polymer in the fabrication of microdevices. It falls under the category of silicones, which are synthetic polymers with a Si-O backbone. PDMS is composed of a repeating $(\text{CH}_3)_2\text{SiO}$ unit, see

Figure 3, and can be produced in various rheological forms, including fluids, emulsions, resins, elastomers, and rubbers, depending on the length of the polymer chain” [36].

“The elastomeric form of commercial PDMS is typically found in a kit that includes a PDMS base solution and a curing agent used to cross-link fluid PDMS with an elastomer. The siloxane base, also known as prepolymer, contains vinyl-terminated end groups ($\text{CH}_2=\text{CH}-$); the base solution also includes a platinum base catalyst and a silica filler. The crosslinking oligomers each contain at least 4-11 silicon hybrid bonds and an inhibitor. The platinum base catalyst catalyzes the addition of the SiH bond across the vinyl group, allowing for 3D cross-linking due to multiple reaction sites on both the monomer chain and the cross-linking chain. This additive reaction is advantageous because it doesn't generate any waste products, such as water. By increasing the ratio of curing agent to base, a harder, more cross-linked elastomer can be obtained” [35].

For the intended use, PDMS boasts a variety of advantageous material properties. Specifically, its surface features a low interfacial free energy, and its superficial properties are straightforward to customize.

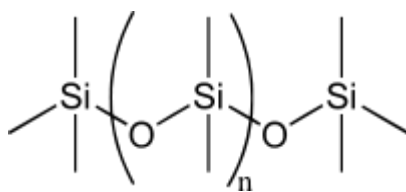


Figure 3- PDMS chemical composition, Wikimedia Commons. (s.f.). The PDMS monomer structure features covalent Si-O bonds, providing stability and flexibility. The siloxane linkage between silicon and oxygen units contributes to PDMS's chemical resistance and biocompatibility.

The most commonly utilized commercial PDMS variant is Sylgard™ 184 (Figure 4), which is produced by Dow Corning and composed of two components: a silicon base and a curing agent. Sylgard™ 184 presents excellent physical attributes, including a high tensile modulus (1.8MPa), high physical toughness (4.77MPa), minimal shrinkage after curing (1.1%), and an elongation capability of up to 160% [35].

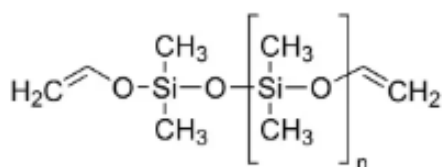


Figure 4- Sigma-Aldrich (s.f.), Sylgard 184 chemical structure. Structure of the Sylgard 184 monomer, which consists of siloxane (Si-O) units with terminal vinyl and methyl groups. This configuration contributes to the polymer's flexibility, durability, and ease of cross-linking in the curing process.

2.5.2 Polystyrene Sulfonate

Polystyrene sulfonate (PSS) is highly water-soluble and may also exhibit certain hydrophobic properties, depending on its chemical structure and concentration. Its water solubility makes it useful in various applications involving water as a solvent or reaction medium. For example, it can be used as a release agent for detaching materials, such as in our case where it was used as a release agent for PDMS on glass wafers.

2.5.3 Polyethylene Terephthalate

“Polyethylene terephthalate (PET) is a thermoplastic polymer resin of the polyester family, synthesized using terephthalic acid (TPA) and ethylene glycol (EG)” [37]. The PET material displays outstanding thermal and mechanical properties. Its melting temperature is 260°C, making it suitable to the temperatures used during depositions. The utilization of the PET shadow mask eliminated the need for using photolithography, which typically necessitates high-quality and often costly masks. The application of the PET mask facilitated a simpler and faster process, eliminating the need for the multi-step procedures associated with photolithography.

During the project, we used the Mylar PET 23 μm as a mask to create patterns for deposition.

2.6 Metals

2.6.1 Gold

Gold is a metal with exceptional chemical properties that render it the most inert metal among all other metallic elements [38], making it highly resistant to oxidation and corrosion. It is renowned as one of the most effective electrical conductors among metals, and it particularly well-suited for applications that involve high-frequency transmissions.

Gold is recognized for its compatibility with biological tissues, and in biomedical applications, it is frequently combined with other materials to enhance its performance and usability. Although gold is one of the most inert metals, it can degrade over time in a biological environment, especially when subjected to varying electrochemical potentials during operation. For instance, in this application it requires encapsulation. The encapsulation acts as a protective barrier against moisture, allowing the entire system to function correctly even when fully immersed in biofluids. It is possible to use conductive polymers as for example PEDOT-PSS (poly(3,4-ethylenedioxythiophene)-poly(styrenesulfonate)), which is a conductive polymer utilized to encase gold-based medical devices or sensors. This polymer offers numerous advantages, including electrical conductivity, biocompatibility, and ease of processing.

2.6.2 Platinum

Platinum, a transition metal, possesses outstanding electrochemical properties attributed to its stability, which prevents easy oxidation in electrochemical environments and resistance to corrosion. These qualities drive the exploration of this material as electrodes that, if proven effective and high-performing, would eliminate the need for encapsulation when interfacing with human tissue.

3 Methods

3.1 Microfabrication

The fabrication process of the test tracks follows a modified version of the protocol presented in [25]. Figure 5 presents the flow chart summarizing the microfabrication process. The figure offers a cross-section of the final design of the tracks.

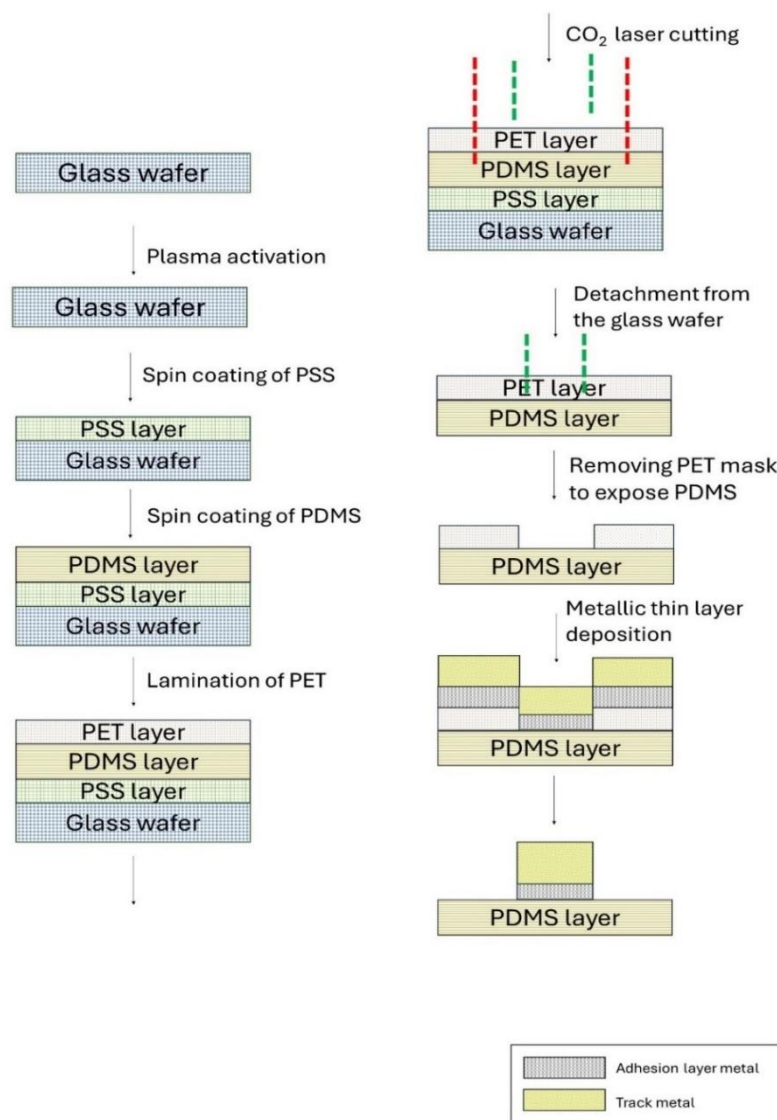


Figure 5- Flowchart of the microfabrication process. The sequence begins with a wafer, followed by the deposition of a PSS layer, a PDMS layer, and a PET layer. A CO₂ laser then creates the deposition pattern, which is subsequently deposited according to the defined design.

The selection of a glass wafer over a silicon wafer was based on the fact that laser cutting parameters had already been optimized for glass wafers. In this instance, the utilization of glass wafers was advantageous due to the transparency of the deposited polymeric materials on their surface. The use of glass wafers also facilitates the observation of impurities or air bubbles, making it easier to detect and correct errors.

To start the production of samples, it's essential to have a basic structure in place. This structure includes three key components, which are as follows: glass wafer, a PSS layer that is spin-coated on top of the glass wafer and acts as an adhesive, it helps to bind the PDMS layer to the glass wafer and facilitates the peeling off of the PDMS from the glass wafer and a PDMS layer that is spin-coated on top of the PSS layer.

3.1.1 Glass Wafer Plasma Activation

When the wafer glass undergoes plasma activation, the surface is altered by the high-energy ions of the plasma, creating active sites that can form covalent bonds. The plasma treatment enhances the hydrophilicity of the wafer surface, improving its interaction with water and facilitating the detachment of the devices in subsequent stages. This modification was necessary to achieve better wettability and improved adhesion of the PSS coating.

Plasma activation of the glass wafer was accomplished using the Plasma Cleaner (PPS). Inside the chamber, the power was adjusted to 30 W, while maintaining an argon flux of 30 sccm. The activation process was executed for 30 seconds.

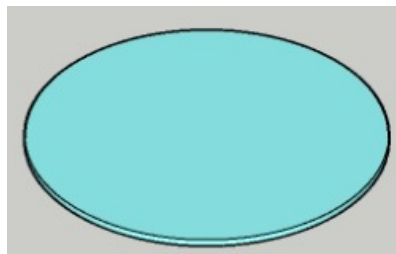


Figure 6- Plasma-activated glass wafer, it shows enhanced surface hydrophilicity for improved adhesion of subsequent layers

3.2.2 PSS Spin Coating

The wafer was coated with PSS Poly(4-styrenesulfonic acid) solution from Sigma-Aldrich, as shown in Figure 7, using the Spinner 2 AB Plast Spin 150 (AB Plast). The coating process involved two stages after pouring the PSS on top of the plasma-activated surface of the glass wafer: first, spin coating for 20 seconds at 100 rpm with an acceleration of 1000 rpm/s, followed by spin coating for 45 seconds at 2000 rpm with the same acceleration rate.

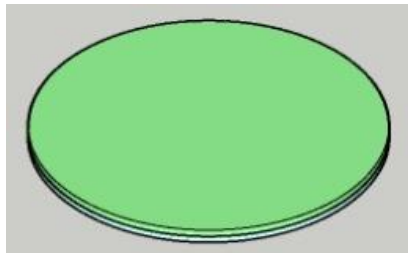


Figure 7- Plasma-activated glass wafer (blue) with a PSS layer (green) applied via spin coating

3.3.3 PDMS Preparation And PDMS Spin Coating

To obtain the required samples, the first step was to prepare the PDMS (Polydimethylsiloxane). This involves using the SYLGARD 184 Elastomer kit, which contains both the elastomeric base and the curing agent. The elastomer kit is typically a two-part system that needs to be mixed in the correct proportions to create a homogeneous mixture. The curing agent mass to pre-polymer mass ratio for the SYLGARD 184 is 1:10, meaning for every 10 grams of pre-polymer, 1 gram of curing agent is required. Approximately 35 grams of pre-polymer and 3.5 grams of curing agent were added based on these proportions. Subsequently, the mixture was transferred to a mixer, which is essential for blending and particularly for eliminating air bubbles that may form. The SpeedMixer™ DAC 150 FVZ-K (Synergy Devices Limited) mixer was utilised to obtain a homogenous mixture without any air bubbles. In this case, the ingredients were mixed in the SpeedMixer for 4 minutes at a speed of 2500rpm, followed by a 10-minute degassing stage. This process enables the production of a final product almost completely free from any air bubbles that could compromise its integrity. The degassing process involves placing the PDMS in a vacuum chamber and applying vacuum for 10 minutes. After the degassing procedure, the air bubbles, if any, were not visibly detectable to the naked eye. However, in the event of any latent air bubbles, they have been eliminated during the spin-coating process of the PDMS upon the wafer.

The process of PDMS deposition involved applying a layer of PDMS onto the wafer, with a thickness that varied from 150 μm to 300 μm . This was achieved using the Spinner 2 AB Plast Spin 150 (AB Plast) and the spin coating technique. The wafer, previously coated with the PSS layer, was securely held in place using vacuum. To ensure a uniform deposition, the PDMS was poured as close as possible to the sample surface to avoid the formation of any air bubbles. The wafer was first spun for 10 seconds at 100 rpm and then for 30 seconds at 800 rpm. Once the coating process was complete, the wafer was cured in an oven at a temperature of 60°C for 2 hours and the structure shown in Figure 8 was obtained.

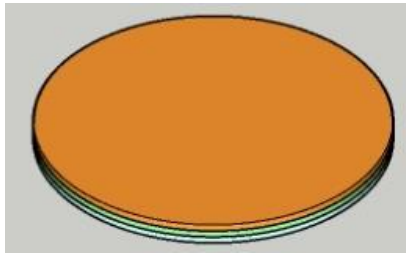


Figure 8- Layered structure showing PDMS (orange) spin-coated over PSS (green) on a plasma-activated glass wafer (blue).

3.3.4 PET Lamination

To create a shadow mask for electrode deposition, it was necessary to laminate a layer of Mylar PET 23 μm onto the PDMS surface to obtain a shadow mask. This process required manual lamination of a PET foil onto the PDMS surface in a clean room environment.

First, the PET roll was unrolled, and the was cut to the appropriate dimensions for the wafer application. Next, the freshly cut layer was cleaned using nitrogen. Then, the PET layer was gently laminated onto the wafer, with careful attention paid to ensuring complete adherence and minimizing the formation of air bubbles between the PDMS and PET layers. If visible air bubbles were present, they were removed by directing the bubbles towards the wafer's edges and releasing them.

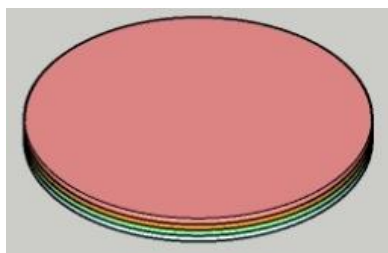


Figure 9- Composite image showing the entire layered structure: glass wafer (blue), PSS layer (green), PDMS layer (orange), and an additional PSS layer (pink) laminated on top

3.3.5 Mask Design And Laser Cutting

Once the base structure was prepared, it was necessary to create the desired pattern for metal deposition. This was achieved by cutting the sample using the Epiloglaser Zing 30W (Epilog Laser), a CO₂ laser. The laser cuts the sample to form the desired pattern by following a customized template.

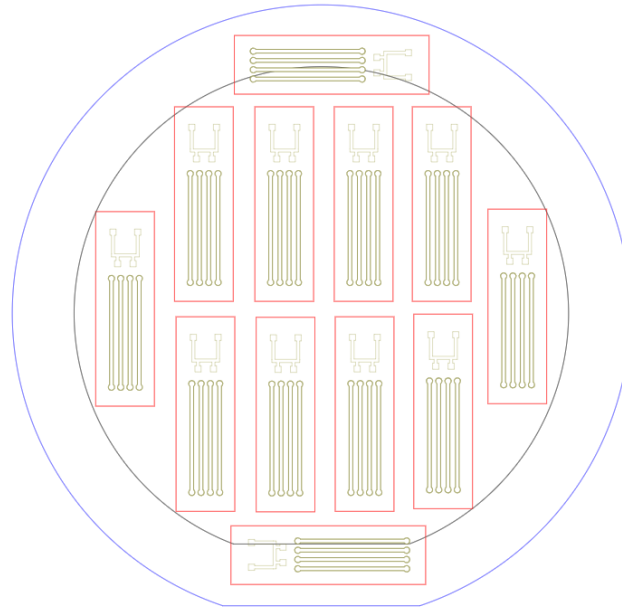


Figure 10- Top view of the wafer mask showing: blue line indicating the wafer perimeter, black line marking the safety perimeter, red lines outlining the testing device perimeters, and green lines defining the individual tracks and bridge perimeters

The mask design has been crafted using Inkscape. It was possible to produce 12 track arrays for each wafer. The wafer that was utilised has a diameter of 4 inches. In Figure 10 the wafer perimeter is outlined by the blue line. The individual devices are demarcated by the red lines and each track is delimited by the green lines. The design was meant to include four tracks for each sample to facilitate the simultaneous simulation of mechanical stress on four different tracks during the testing process, in order to improve the yield of the test results.

In addition, each sample was fitted with a bridge design to allow us being able to assess the sheet resistance for each device after the detachment of each sample from the wafer before undergoing different deposition processes.

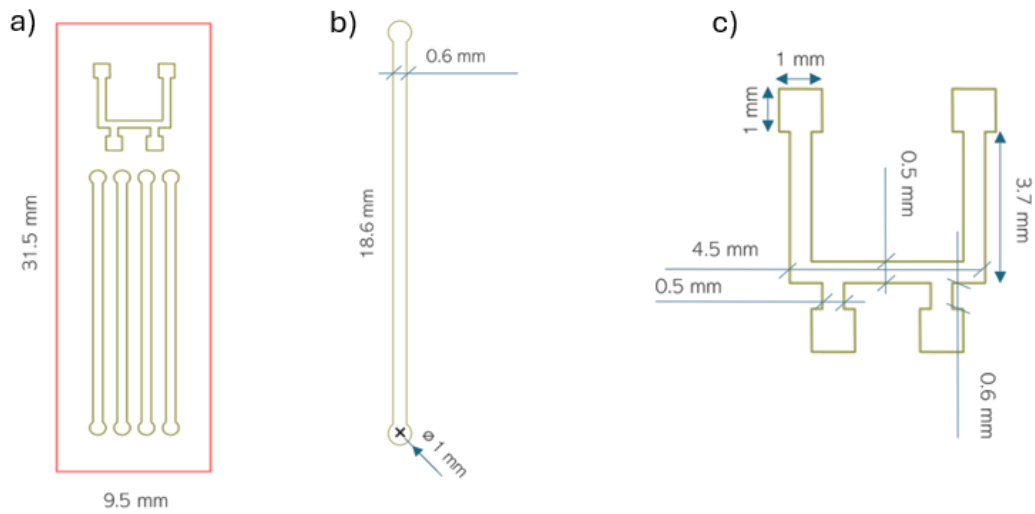


Figure 11- Top view of the wafer mask showing: a) test device designs with red lines outlining their perimeters; b) individual track designs with green lines defining their boundaries; and c) bridge test structure design, also outlined in green

We have discovered through bibliographic research that generally most of the cuff electrodes would be 7-20 mm in length [39] and the track width would be between 0,5 and 2mm [40] so we adjusted the design of the mask with these measures as shown in Figure 11.

By adjusting the speed and power of the laser it was possible to obtain cuts with specific depths. Figure 10 above exhibits four different colours that served as input for the CO₂ laser to carry out a different range of cuts. In the following paragraphs, the different cuts will be illustrated. The deposition has to occur on the PDMS surface. To achieve this, the PDMS surface must be exposed only on the areas of the substrate where the metals are intended to be deposited. The red dots in the figures below are indicative of the position of the laser pointer. In Figure 10, the overall mask design is shown. To better visualize the cuts, next to each cut-describing picture, the overall mask is represented.

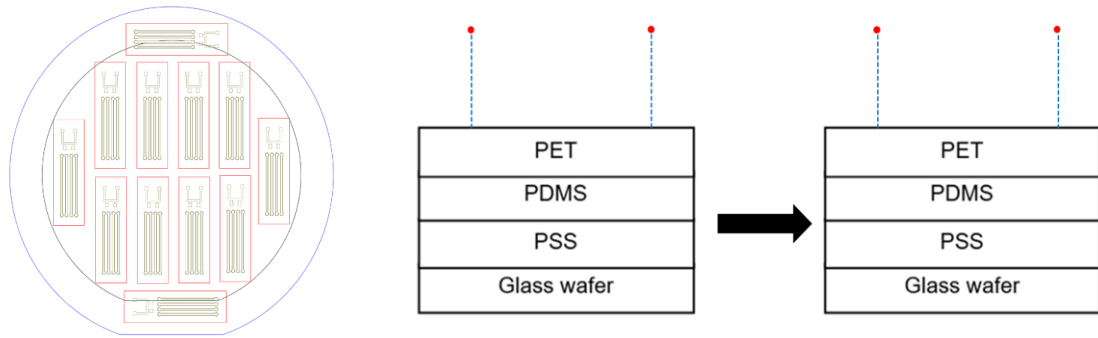


Figure 12- Left: The full mask with a continuous blue line denoting the wafer perimeter. Right: Side view of the different layers, showing that the laser, represented by the dashed blue line, does not penetrate or cut through the layers.

As shown in Figure 12 on the left, the blue line indicates the perimeter of the wafer. This blue line was crucial as it provided a guide for aligning the wafer precisely with the laser point. During this initial stage, the laser power was set to zero, meaning it only illuminated the wafer's perimeter without making any cuts. This approach allowed us to visually verify the alignment of the wafer without risking any damage or misalignment. In Figure 12 on the right, the non-continuous blue line represents the alignment cut. This line does not penetrate or cut the surface of the wafer, ensuring that the wafer was aligned correctly before the actual cutting process began. This method was employed to confirm that the wafer was positioned accurately relative to the laser, which is essential for maintaining precision and avoiding errors in the subsequent cutting steps.

The black line in Figure 10 indicates the safety perimeter of the wafer, calculated with a 1 cm internal offset from the wafer perimeter. Beyond this line, the wafer may not be used as the samples might be defective or inadequately cut. In our case, if the alignment was not precise, there was a risk that the cutting of samples outside the safety zone may not have been completed. Although the black line was designated as a safety measure, we decided to utilize the space outside the safety margin to reduce material waste. The primary objective was to minimize the quantity of unused material, which would have otherwise resulted in increased costs. This line wasn't used as input for the CO₂ laser but is generally a common practice in mask design to account for this safety boundary.

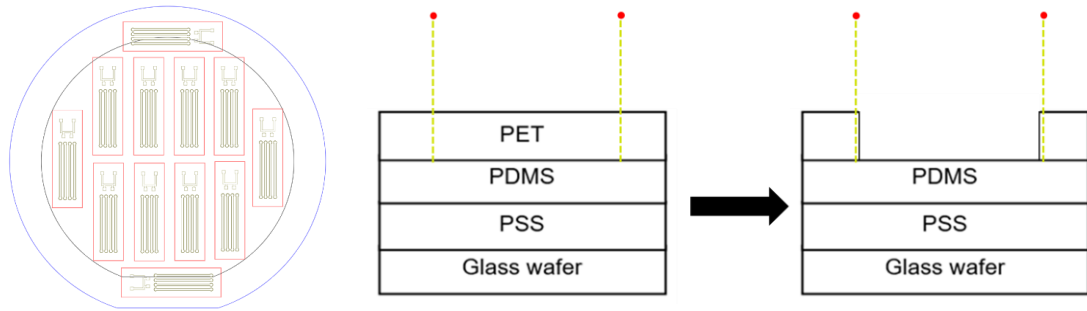


Figure 13- Left: The full mask with continuous green lines outlining the tracks. Right: Side view showing the green dashed line representing the cut that penetrates the PET layer, with an arrow indicating the removal of the cut section to expose the underlying PDMS surface.

The green lines in Figure 13 on the left represent the cutting guide to expose the PDMS surface for metal deposition. By cutting along these lines, it was possible to remove the layer on top of the PDMS and expose it. The PET layer was used as a shadow mask to create the desired pattern, allowing metals to be deposited onto the PDMS surface. Figure 13 on the right shows how the laser cut through the PET layer that was consequently peeled off to reveal the PDMS surface.

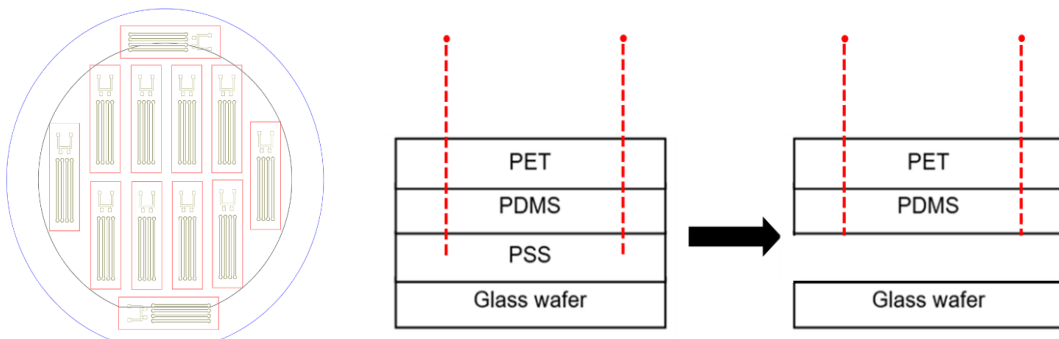





Figure 14- Left: The image displays the full mask with red continuous lines outlining the perimeter of each device. Right: The red dashed line represents the cut necessary to detach the devices from the wafer. This cut penetrates both the PET and PDMS layers. The arrow indicates that this cut will facilitate the removal of the devices from the wafer, enabling their separation from the wafer.

The red lines in Figure 14 have been designed to provide the singulation of each testing device: each sample has to be self-standing, which means it has to be detached from the glass support. The laser made precise incisions through the PET, PDMS layer, and a portion of the PSS layer as it is possible to see from Figure 14 on

the right. This allowed for the detachment of the sample from the glass wafer with ease and accuracy in the following step.

The CO₂ laser cutting technology and the PET shadow mask were chosen for the process's lower cost and more rapid microstructures' fabrication when compared to the conventional time-consuming photolithography process [41].

Table 1- Parameters for the described cuts, including alignment (blue lines), track cuts (green lines), and device detachment (red lines). Power and speed are shown as percentages of their maximum values, with the laser's max power being 30W. Maximum speed was not provided in the tool manual.

	Power	Speed	Frequency (Hz)
Cut 1 	0	100	280
Cut 2 	1	10	280
Cut 3 	2	10	280

In Table 1 are listed the set parameters for each of the previously described cuts. The power and speed parameters are represented as a percentage of their respective maximum values. The laser's maximum power is 30W, although the maximum speed value was not identified in the tool manual.

After the cutting the wafer looks how it is showed in the Figure 15.

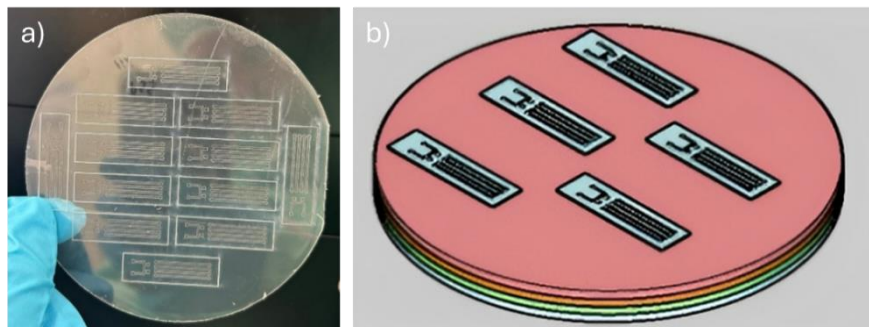


Figure 15- (a) Image of the cut wafer. (b) Close-up of the white cut on the PET/PDMS/PSS/glass wafer structure, illustrating the incision through the layered materials

3.3.6 Detachment From The Glass Substrate

The aim of this project is to study the stretchability of tracks featuring a PDMS-metal layer-PDMS configuration. At this stage of the fabrication process, the PDMS devices are still stuck on top of a glass wafer.

To facilitate the use of different deposition types and parameters for every sample, it became necessary to separate the twelve samples from the wafer before deposition so that each one of them could undergo different deposition techniques and parameters. To achieve this, the cut glass wafer was placed in a container with distilled water for one hour to dissolve the PSS release layer and thereby detach the PDMS/PET layer from the glass wafer, and the individual samples were extracted from the wafer following the laser-cut markings using sharp tweezers as it is possible to see from Figure 16.

The samples underwent a drying process on a hot plate set at 70°C for 10 minutes to remove residual water and moisture.

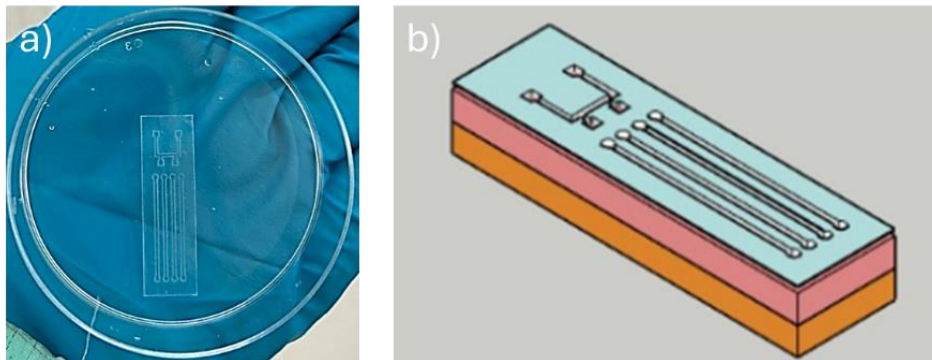


Figure 16- (a) Image of a single sample detached from the glass wafer. (b) View of the sample, showing the layers from bottom to top: PDMS layer, PET layer, and the cuts.

3.3.7 Peeling Off The Cut PET Mask

The previously cut PET mask was removed as shown in Figure 13 on the left using tweezers to reveal the PDMS surface onto which the metal will be deposited. PDMS is a highly adhesive and tacky material. Therefore, despite being in a clean room environment, to prevent dirt from depositing on the surface where the deposition will take place, causing contamination and delamination issues of the metal from the polymer, this process of removing the PET mask was done immediately prior to deposition.

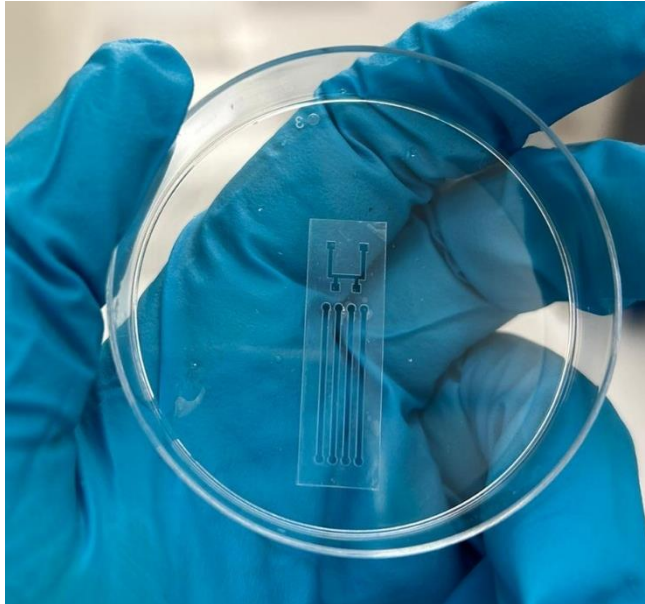


Figure 17- Sample after detaching the cut PET mask, which reveals the underlying pattern of tracks and bridges. The image shows the structure of the tracks and bridges as designed, now visible on the surface of the sample following the removal of the masking layer.

3.3.8 Deposition

During this step, a thin metallic layer was deposited on the surface of the sample, which, at this point in the microfabrication process, comprises a layer of PDMS and the cut PET mask as shown in Figure 17. A support wafer was used to accomplish the deposition. The sample was positioned on top of the test wafer with the side with the PET mask facing up as the deposition process must occur on this side of the sample.

Kapton tape was applied to the perimeter of the sample to secure it in place on the support wafer before placing it in the deposition chamber.

Each deposition involved the deposition of only one single sample at a time.

3.3.8.1 Thermal Deposition

The process of thermal deposition was executed using the Thermal Evaporator Moorfield MiniLab T25M (Moorfield Associates). This tool allows for the simultaneous deposition of four different metals in each cycle. Seeds of gold and chromium metals were inserted into Al_2O_3 crucibles before being attached to the structure.

After positioning the support wafer with the samples facing downwards on the chamber, it was securely sealed, and it was necessary to wait for the chamber to reach the ideal pressure for deposition, which typically took four to six hours. The entire process was executed under a pressure range of $2 \cdot 10^{-6}$ to $5 \cdot 10^{-6}$ bar.

The deposition process started by modulating the voltage with a knob. A display showed the current value, allowing for control of both voltage and current parameters to achieve different deposition rates. The voltage and current were gradually incremented to prevent damage to both the sample and machinery and avoid sudden spikes in deposition rate values.

As the deposition progresses, the chamber heats up. Heat is utilized as the means for metal evaporation in this deposition process. As the tool lacks an integrated

temperature sensor to monitor the temperature within the chamber, a thermometric strip was taped on top of the wafer support. The adhesive sensor didn't provide real-time temperature readings, but it did indicate the maximum temperature reached inside the chamber. The temperature is a crucial factor that requires monitoring, especially when dealing with polymers, due to the coefficient of thermal expansion, which is significant for polymers. This specifically may affect the metal structure after the deposition, eventually providing a flatter surface at lower temperatures and a wrinkled surface at higher temperatures. The sensor used had a minimum threshold of 70°C, meaning that if the internal temperature reached 70°C, the 70°C indicator would light up. However, during all deposition processes, the indicator never turned on, confirming that the temperature inside the chamber consistently remained below 70°C. To protect the sensor from being coated by metal layers, it was coated with tape. The tape was later removed to read the maximum temperature attained inside the chamber.

Table 2 shows the applied voltage, current, and resulting deposition rates for chromium and gold layers under the specified conditions.

Table 2: Deposition parameters for chromium and gold using thermal evaporation, including voltage, current, and deposition rates. The chamber temperature was below 70°C for each deposition.

Metal	Voltage (V)	Current (A)	Deposition Rate (Å/s)
<i>Chromium</i>	110	26	0.1
<i>Gold</i>	120	28	0.65

3.8.2 Sputtering Deposition

The deposition of the thin layers through the sputtering technique was achieved by using the Sputter AJA (AJA International Inc.).

First, the sample-containing wafer was placed face down in a small chamber and the pressure was reduced to below 10^{-6} torr in few minutes before transferring it to the reaction chamber. After selecting the correct material for the thickness-sensor, a specific power value and argon flow rate were set. These values can be found in literature or, in this case, were taken from a notebook of previous experiments conducted by other instructors or students. Once the power and argon flow rate values were set, the wafer was rotated for achieving a better uniformity of the deposition.

The chamber pressure was not considered a variable parameter because the equilibrium pressure for all depositions ranged between $4.8 \cdot 10^{-3}$ Torr and $5.5 \cdot 10^{-3}$ Torr.

Table 3 outlines the power settings, argon flow rates, deposition rates, and target thicknesses for each metal deposition process.

Table 3- Deposition parameters for thin layers using the sputtering technique, including power settings, argon flow rates, deposition rates, and target thicknesses for each metal.

Metal	Power (W)	Argon Flow (sccm)	Deposition Rate (Å/s)	Thickness (nm)
<i>Chromium</i>	60	14	0.1	7
<i>Gold</i>	80	10	0.65	40
<i>Titanium</i>	90	8	0.1	7
<i>Platinum</i>	150	10	0.16	40

During the deposition, the metal layer was deposited on the exposed PDMS surface, while the majority was oversprayed, settling on the PET mask. The PET mask was removed and discarded in the following step.

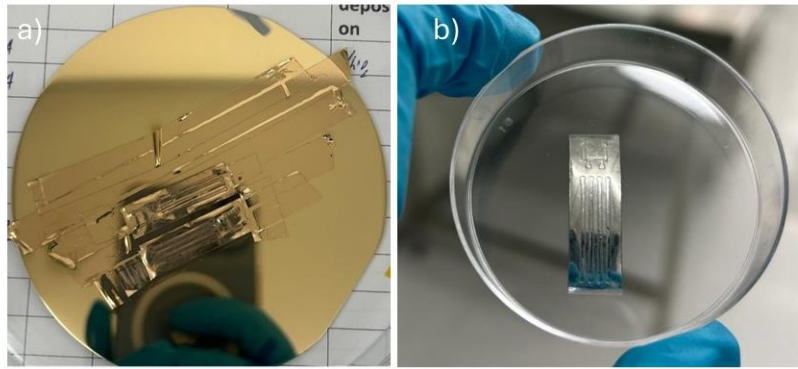


Figure 18- Deposited metal on the support wafer and sample immediately following the deposition process. (a) Gold deposited on the support wafer and on the entire sample, and (b) Platinum deposited on the entire sample.

3.3.9 Peeling Off The PET Mask

Once the deposition process was complete, the remaining PET mask was removed with ease using a pair of tweezers, allowing the sample to be revealed as shown in Figure 19.

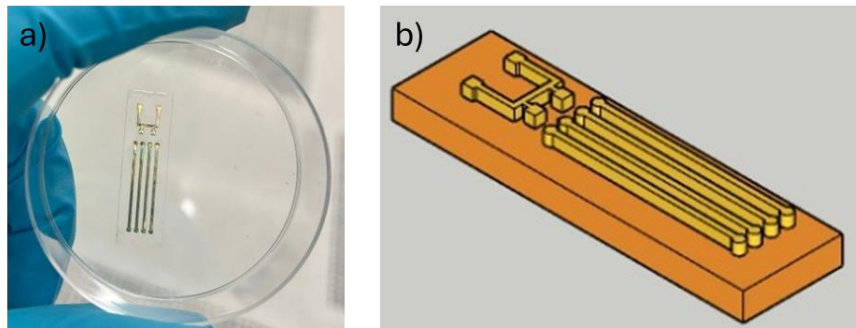


Figure 19, Sample after the PET mask detachment: revealing of the deposition pattern.

In this phase of the microfabrication process, the sample's resistance was assessed, and it was examined under a microscope. The resulting structures varied depending on the types of deposition and the established parameters. These structures have been identified using advanced instruments such as SEM, as well as with a basic optical microscope.

3.2 Encapsulation and interconnections

The encapsulation process consisted of establishing interconnections to measure the tracks' resistance during the stretch test.

Due to the delicacy of the samples, care was taken to prevent any damage or additional cracks on the samples. To achieve this objective, the samples were transferred only once onto a glass petri dish before the encapsulation process. Subsequently, the entire encapsulation procedure was carried out on this support to minimise any unnecessary movement of the tracks.

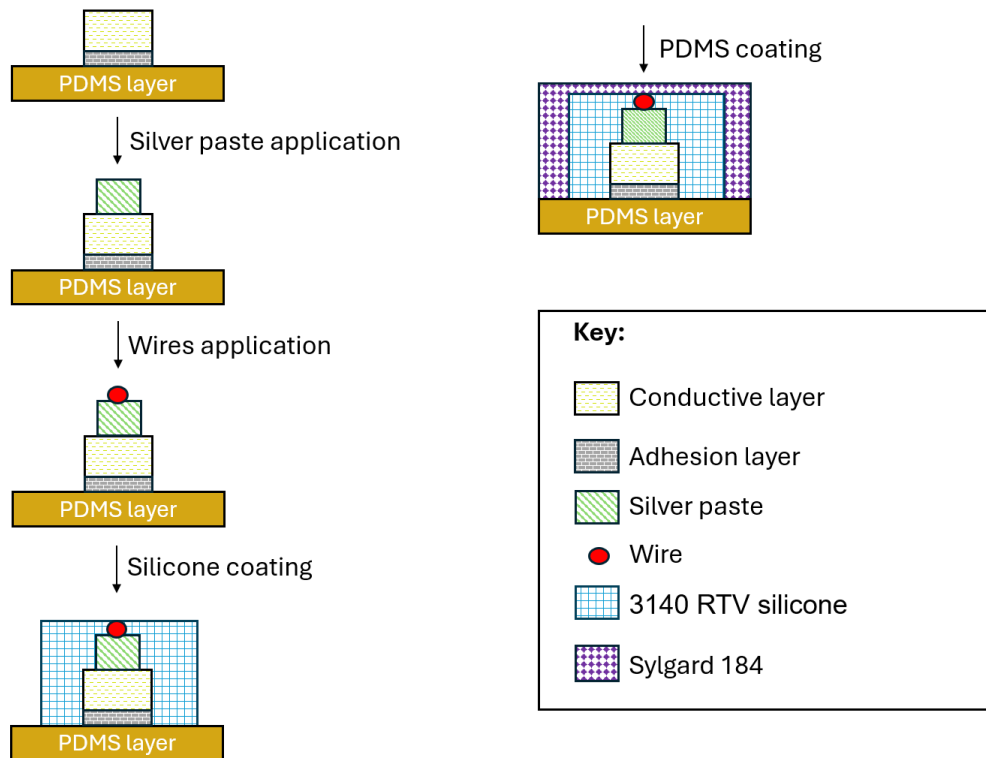


Figure 20- Flowchart depicting the process for creating and protecting electrical interconnections on samples. The images illustrate the sagittal plane of the samples throughout the different stages: (1) Application of silver conductive paste (Elcolit 325) to the edges of the metal tracks; (2) Wires application in correspondence with the silver paste; (3) Application of silicone layer environmental protection and electrical insulation; (4) PDMS coating process of the tracks.

3.2.1 Silver Paste Application

To achieve the interconnections, a silver conductive paste, the Elcolit 325, was applied along the edges of the tracks. Elcolit 325 is a two-component electrically conductive epoxy adhesive that is mixed in a 1:1 ratio by mass before application. Following the preparation of the paste with 1 gram of each component, it was carefully applied on the tracks edges using a thin, rounded needle and an optical microscope.

Then, the wires were carefully placed onto the paste, as shown in Figure 21.

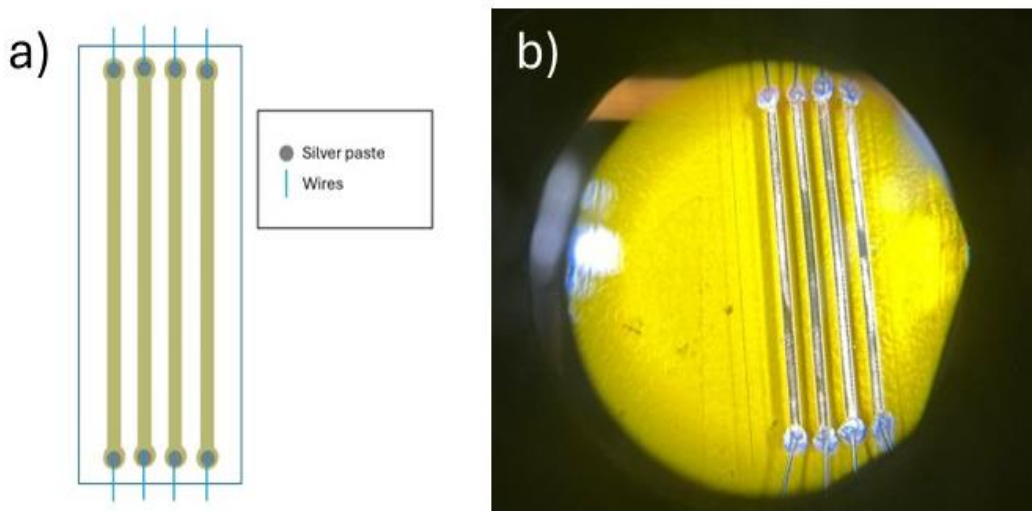


Figure 21- Wires application process. (a) Schematic of the silver conductive paste (Elcolit 325) applied along the edges of the tracks, with wires placed on the paste. (b) Microscope image showing the detailed application of the paste and wire placement on the tracks.

After applying the wires, the samples were placed in an oven at 60°C for 2 hours to cure the paste as specified on the paste datasheet.

3.2.2 Silicone Application

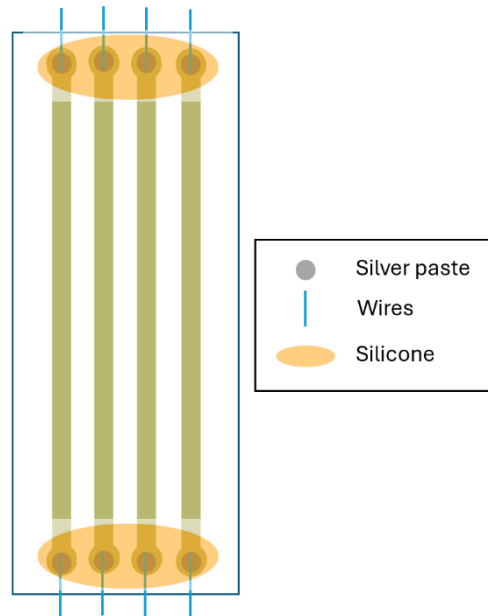


Figure 22- Top view of the device with the silver conductive paste (Elcolit 325) applied along the edges of the tracks, with wires placed on the paste and a silicone layer applied for protection and insulation, using 3140 RTV from DOW CORNING®.

After applying the silver conductive paste, a layer of silicone was added (see Figure 22) to protect the interconnection against moisture, dust, chemical contaminants, and other environmental factors that could damage electronic components and circuits. Additionally, it offers excellent electrical insulation properties, safeguarding circuits from short circuits and other electrical issues. Specifically, we applied the 3140 RTV coating from DOW CORNING®, which is a non-corrosive silicone rubber that easily flows and solidifies upon contact with moisture. To initiate the vulcanization process, a small droplet of water was placed near the sample and left undisturbed for 24 hours.

3.3.3 PDMS Coating

After the interconnection process was completed, a layer of PDMS was applied to all the tracks, ensuring that the interconnection points remained free from the coating. The final design should look like the one represented in Figure 23 .

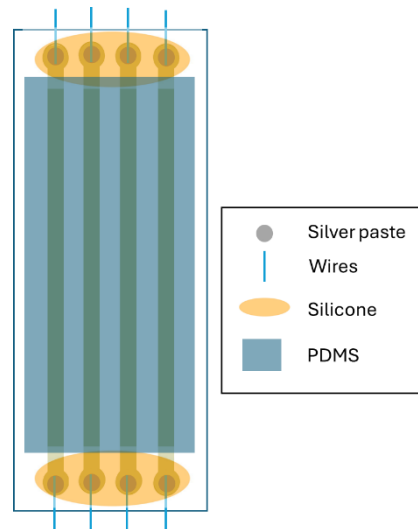


Figure 23- Final design with PDMS coating, leaving interconnection points exposed

The PDMS encapsulation was done at first using spin coating, but it was necessary to lift the wires above the wafer surface to prevent them from being covered by PDMS. To ensure even distribution of the PDMS on the samples, the wafer was spun at 100 rpm for 10 seconds and then at 800 rpm for 30 seconds before curing at 60°C for 2 hours, as per previous methods. However, this method resulted in non-conductive tracks due to damage of the interconnections incurred during the lifting of the wires and the spin coating.

To solve the issue, a 3D-printed mould that matched the design of the samples was created, see Figure 24. This mould provided a casting system, and by applying some drops of PDMS in the middle of the cast and applying it carefully with a rigid support, the tracks were encapsulated with a PDMS layer approximately 300 μm thick, similar to the mould thickness. The mould was placed on the sample, PDMS was poured, and a rigid cardboard was used to evenly spread it on the sample manually.

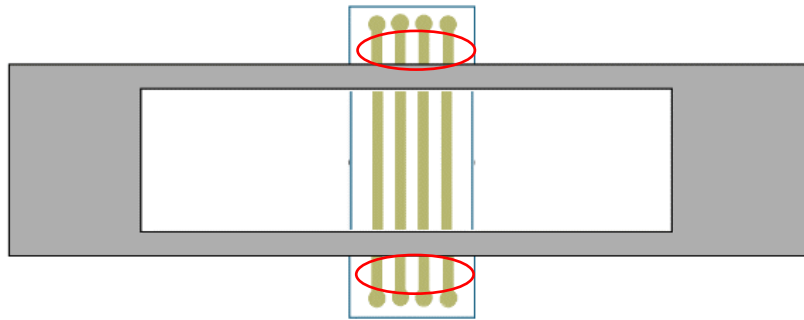


Figure 24- Top view of the 3D-printed mould system used for PDMS encapsulation. The mould ensures an even PDMS layer of approximately 300 μm thickness. The red circle highlights the intentional gaps of about 5 mm left on both sides of the resistance measurement points to accommodate potential PDMS leakage.

As it is possible to see from the Figure 24 in the red circle while designing the mould, a gap (approximately 5mm) was intentionally left on both sides between the resistance measurement points (located at the ends of the tracks) and the coated part of the tracks. This precautionary measure was taken to allow for a safety margin in the event of PDMS leakage under the mould.

After this step, the samples were ready to undergo the mechanical tests.

3.3 Samples Characterization

Sample characterization was conducted before testing to assess the success of the deposition process, to detect any macro and microcracks resulting from deposition and to establish a baseline for comparison post-testing.

3.3.1 Optical Microscopy And SEM Analysis

To conduct optical microscopy, the Leica DM4000M Optical Microscope (Leica Microsystems) was used. The samples were positioned on a support wafer and analyzed through both the microscope's eyepieces and computer imaging. By doing so, it has been possible to acquire detailed images and obtain indicative measurements that helped us evaluate the impact of different deposition techniques and temperatures on the cracks and wrinkling of the surface.

For the scanning electron microscopy (SEM) analysis, we utilized the SEM Hitachi SU 3500 (Hitachi) and the SEM Hitachi SU 8230 (Hitachi). The samples were affixed to a support using double-sided copper tape and then introduced into the SEM device.

“Surface charging was observed during sample examination due to the PDMS's nonconductive properties. Charging occurs when there are excessive electrons accumulated on the sample surface, which is impinged by an electron beam; the accumulation of electrons on the sample surface builds up charged regions. In these regions, electric charges generate distortion and artefacts in SEM because they irregularly deflect the incident electron probe during scanning. Moreover, charging alters SE emission, and causes the instability of signal electrons. Charging is generally not a problem for metallic samples because their good electrical conduction ensures the removal of excess electrons. While regarding the SEM analysis of metal layer and non-conductive substrate samples, surface charging is a problem that must be taken into account [42]”.

To mitigate the charging issue stemming from the PDMS substrate, the tracks were grounded by employing one-sided copper tape between the holder and the samples

to establish a connection between the metal tracks and the conductive holder, as illustrated in Figure 25.

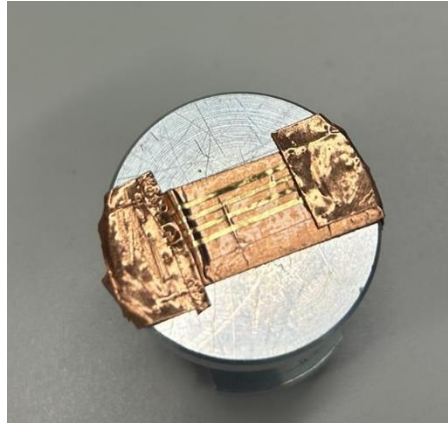


Figure 25- Sample positioned on the support wafer and grounded with copper tape for SEM analysis.

To insert the samples into the tool, the height of the sample was accurately measured to ensure that the stage holding the sample moved as close as possible to the electron beam without, however, impacting the device itself. Upon securing the sample in position, the vacuum parameters were configured: the SEM entails the establishment of a vacuum and precise adjustment of critical parameters, such as beam power and spot intensity, to attain optimal focus. In order to capture the images, we utilized both the secondary electron (SE) and backscattered electron (BSE) modes. We employed the lowest possible acceleration voltages for reducing noise and minimizing charging effects.

3.3.2 Four Probes Resistance Measurements

The Keysight 35561A (Keysight) multimeter was utilized to perform 4-probe resistance measurements with the 4-probe measurement setting. The objective was to evaluate the sheet resistance of thin layers in Ω/square by applying current through two outer probes and measuring the voltage across the two inner probes.

Before the stretching test, the conductivity was assessed by measuring the resistance of the bridges and tracks with rounded needles.

3.4 Mechanical Stretch Testing

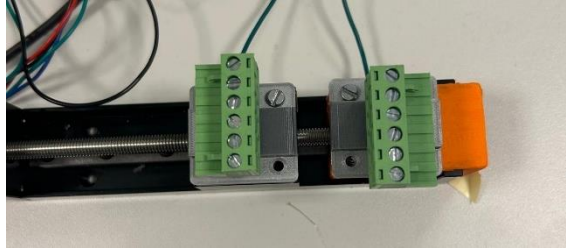


Figure 26- Sample secured for cyclic tension testing. The setup includes a stepper motor and two 3D-printed supports with double-sided tape to hold the sample in place.

The sample underwent cyclic tension testing to measure its resistance, which allowed for the estimation of the sample's stretchability in terms of an increase in the resistance.

In order to carry out mechanical tests, a stepper motor was utilized, and two 3D-printed supports were positioned on either side to hold the samples securely in place. The support for the mechanical testing tool consists of three parts: two connected to the stepper motor with a magnet and one that attaches to the other ones. These components worked together to assist in the mounting of the sample. To secure the samples in place and prevent movement during the tensile tests, double-sided tape was stuck to the supports connected to the stepper. Before testing, the length of the sample was measured and entered into the script, which then adjusted the supports. The specimen was affixed at both ends and rigidly supported by employing the third element of the support. Once the sample was supposed to be in a relaxed position, which was assessed visually, the support was removed, and the sample was left suspended in place as shown in the Figure 27.

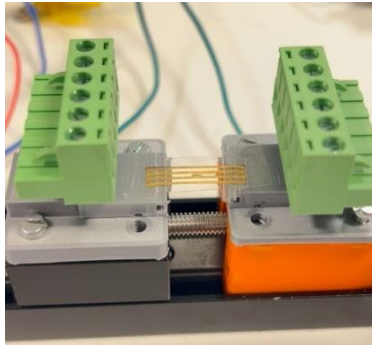


Figure 27- Setup for mechanical testing of the sample using a stepper motor and 3D-printed supports (in green). The supports, equipped with double-sided tape for stability, secure the sample in place.

The Labview script provided the option to customize the number of steps, stretching length value, and number of stretching cycles. The resistance measurements were taken using the Keysight 35561A multimeter and measured twice to ensure a valuable measurement. The measurement was taken by positioning the two probes on each side of the exposed part resulting after the PDMS coating process described in [3.3.3 PDMS Coating](#).

The resistances were recorded after the script completed the specified number of traction cycles. This means that the resistance measurements were taken while the track was in a relaxed state.

3.5 Depositions

Table 4- Summary of deposition parameters for each sample, including material, deposition technique, temperature, and other relevant conditions.

	Adhesion material	Conductive material	Deposition technique	Temperature (°C)
CrAu_T	Chromium	Gold	Thermal evaporation	*
CrAu_S_RT	Chromium	Gold	Sputtering	Room temperature
CrAu_S_70	Chromium	Gold	Sputtering	70
TiPt_S_RT	Titanium	Platinum	Sputtering	Room temperature
TiPt_S_50	Titanium	Platinum	Sputtering	50
TiPt_S_70	Titanium	Platinum	Sputtering	70

Table 4 lists the conducted depositions, with each sample named based on the adhesion layer and the track materials, deposition technique, and temperature. In the following paragraphs, we will use the abbreviated names from the table for convenience.

The deposition parameters to consider during the sample analysis include the deposited metal, deposition method, metallization thickness, chamber pressure, temperature, and deposition rate. The deposition technique was always the same for the conductive and adhesion layers.

Table 5- Deposition parameters for Cr (Chromium) and Au (Gold) layers on a substrate. The table lists deposition rates in Å/s for Chromium (Cr) and Gold (Au), the target film thickness (in Å), chamber pressure (in bar), and the process temperature.

	Cr deposition rate (Å/s)	Au deposition rate (Å/s)	Cr thickness (Å)	Au thickness (Å)	Chamber pressure (bar)	Temperature
CrAu_T	0,1	0,65	65	400	$(2-5) \cdot 10^{-6}$	*
CrAu_S_RT	0,1	0,65	65	400	$(2-5) \cdot 10^{-6}$	RT
CrAu_S_70	0,1	0,65	65	400	$(64-73) \cdot 10^{-3}$	70°C

In the case of the gold samples deposited using the sputtering technique, the constant parameters were the deposition rate, chamber pressure, and layers' thickness, while the variable parameter was temperature, see Table 5.

To compare the gold samples deposited using sputtering to those deposited via thermal evaporation, the deposition rates and layers thickness were kept constant. However, the parameters that varied were the deposition technique, pressure (as thermal evaporation requires higher pressures), and temperature (which, in the case of thermal evaporation, is not constant* and represents the source through which the material is expelled from the target and conveyed towards the substrate), see Table 5. During the process of thermal evaporation, precise temperature monitoring was not conducted throughout the deposition. However, the utilization of a temperature sensor, as detailed in 3.3.8.1 Thermal Deposition, proves the evidence that the temperature never exceeded 70°C.

Table 6- Deposition parameters for Ti (Titanium) and Pt (Platinum) layers on a substrate. The table shows deposition rates in Å/s for Titanium (Ti) and Platinum (Pt), the target film thickness (in Å), chamber pressure (in bar), and the process temperature.

	Ti deposition rate (Å/s)	Pt deposition rate (Å/s)	Ti Thickness (Å)	Pt thickness (Å)	Chamber pressure (bar)	Temperature
	0,1	0,16	65	400	$(64-73) \cdot 10^{-3}$	RT
TiPt_S_50	0,1	0,16	65	400	$(64-73) \cdot 10^{-3}$	50°C
TiPt_S_70	0,1	0,16	65	400	$(64-73) \cdot 10^{-3}$	70°C

Regarding the comparison between the platinum samples, the deposition rate, thickness, and pressure were kept constant. The only parameter that changed during the deposition of platinum was temperature, see Table 6.

For the comparison between gold and platinum samples, the thickness and deposition pressure were kept constant, while the deposition rate for platinum was much lower compared to gold, see Table 5 and Table 6. The reason for this is that achieving an equivalent deposition rate for platinum as for gold would require a significantly higher amount of power which is explained by considering the refractory, or heat-resistant, nature of platinum.

4. Results

4.1 Optical Microscopy

Initially, optical microscopy was conducted on the samples using the optical microscope, which was magnified at 50, 100, and 200 times. Through this analysis, it was possible to discern the differences between the various samples and reveal their surface characteristics.

4.1.1 CrAu_S_R

Figure 28 illustrates the structure of the gold tracks sputtered at room temperature. The image features one of the four tracks of the sample, revealing the CO₂ laser cuts on the sample's sides, the PDMS on the left side, and the metallization at the centre. Gold sputtered at room temperature exhibits very fine cracks arranged in an articulated network immediately after deposition. Based on the image, it is possible to notice that the cracks do not exhibit a single specific directional pattern but rather tend to propagate horizontally and at an approximate angle of 45° relative to the horizontal axis. The pattern was consistent across all CrAu_S_Rt samples.

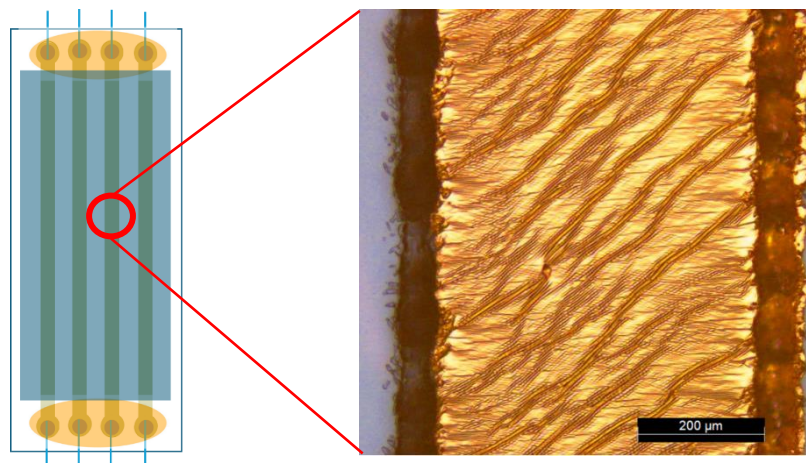


Figure 28- Microscope top view of the CrAu_S_RT sample, showing one of the four gold tracks sputtered at room temperature. The image highlights CO₂ laser cuts on the sample's edges, with PDMS on the left and gold metallization in the center. Fine cracks form an intricate, non-directional network, propagating mainly horizontally and at approximately 45° angles, a pattern observed across all CrAu_S_RT samples

The width of the cracks was measured using the optical microscope, see Figure 28: the results revealed that the majority of cracks had a width of approximately 3 μm on average, with few cracks that stood out due to their larger size, reaching a maximum width of 5 μm .

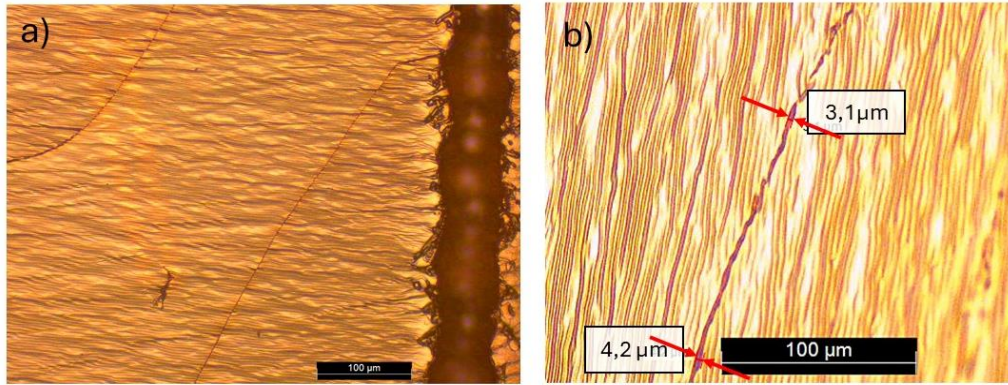


Figure 28- Microscope top view of the CrAu_S_RT sample. (a) Example of an analyzed crack, (b) Measurement of crack widths, showing a crack with a width of approximately 3 to 4 μm .

4.1.2 CrAu_S_70

Every gold sample that was sputtered while subjected to the thermal stage (70°C) developed wider cracks along the geometric axes of the tracks. The width of these cracks, as visible in the Figure 29, appears wider than the horizontal ones. Furthermore, the cracks seem to be superficial, as it's possible to observe the presence of a metallic layer beneath them.

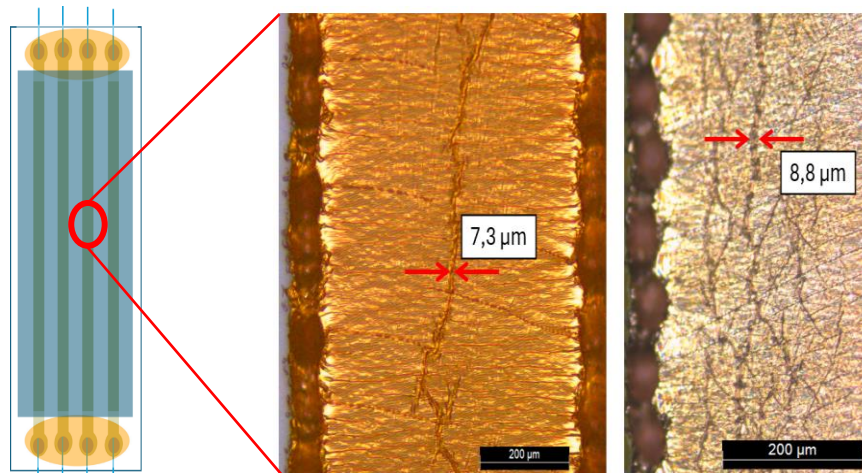


Figure 29- Microscope view of the CrAu_S_70 sample, showing cracks formed after thermal treatment on two different tracks from different devices. The cracks along the geometric axes of the tracks are wider than the horizontal ones.

4.1.3 CrAu_T

In gold samples deposited via thermal evaporation, the surface cracks mainly propagate horizontally, differing from the sputtered samples where cracks occur at a 45° angle. Furthermore, the cracks in the thermally evaporated samples expand at smaller angles compared to those in the samples sputtered at room temperature. The thermal evaporation technique employed for gold deposition exhibits non-uniformity. Examination of the images revealed areas devoid of deposition, manifesting as discontinuities or voids, see Figure 30.

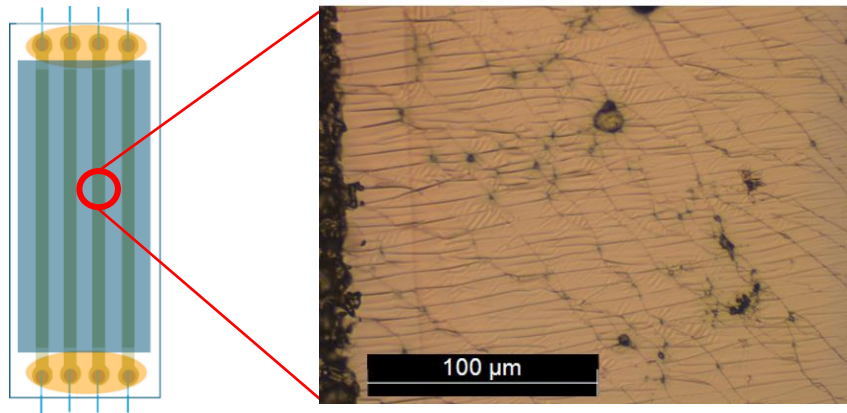


Figure 30- Microscope view of the CrAu_T sample, showing surface cracks formed after gold deposition via thermal evaporation. The image also highlights discontinuities and voids due to non-uniform deposition, with certain areas lacking gold coverage.

Additionally, upon analyzing the images, it is evident that the cracks resulting from the thermal evaporation technique are smaller in width than the sputtering technique. On average, the cracks measure 2 μm, see Figure 31.

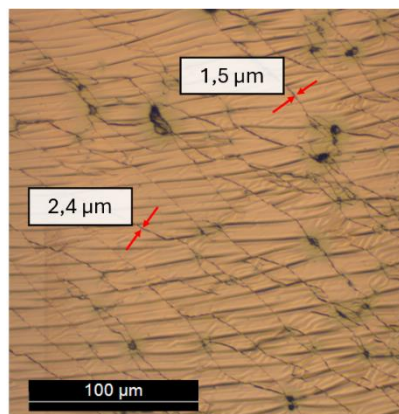


Figure 31- Microscope view of the CrAu_T sample, highlighting the smaller crack widths resulting from gold deposition via thermal evaporation. On average, the cracks measure approximately 2 μm, which is narrower compared to those formed in sputtered samples.

4.1.4 TiPt_S_RT

The platinum samples exhibited noticeable differences when deposited with different deposition parameters. Samples prepared using the thermal stage displayed a more wrinkled and undulated surface compared to those sputtered at room temperature. The platinum tracks deposited at room temperature displayed a remarkably flat surface in comparison to the gold samples that underwent sputtering at an equivalent temperature. Additionally, the platinum tracks demonstrated a lower density of cracks compared to the gold ones. The cracks observed in the platinum electrodes were wider, approximately five times larger, and were arranged in a distinctive striped pattern that spanned the entirety of the sample.

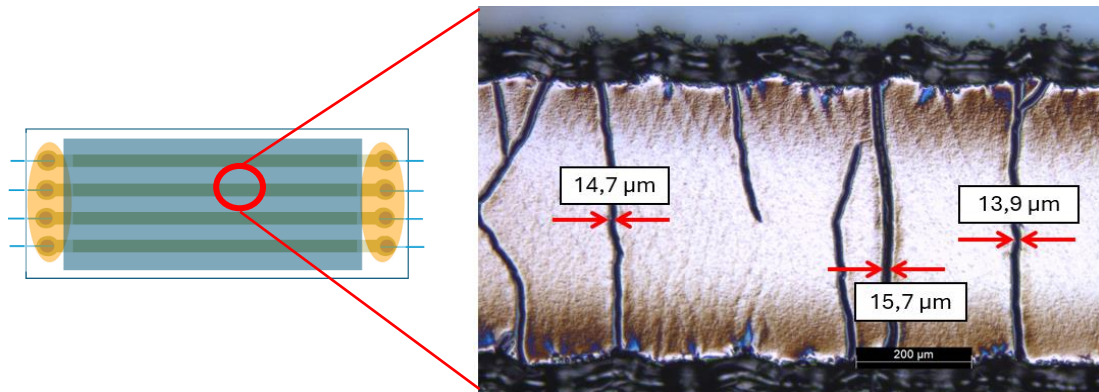


Figure 32- Microscope top view of the TiPt_S_RT sample, showing platinum tracks deposited at room temperature. The image illustrates a notably flat surface with fewer and wider cracks compared to gold samples deposited under similar conditions. The cracks, approximately five times larger than those in gold samples, are arranged in a distinctive striped pattern across the entire sample. Measurements of crack widths are also displayed.

The platinum-sputtered samples at room temperature exhibited a lower deposition density and poor uniformity; the porous properties of the surface are visible under the microscope.

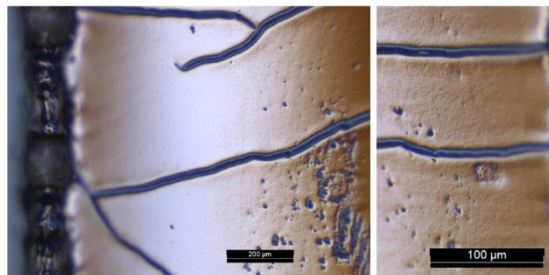


Figure 33- Microscope view of the TiPt_S_RT sample, showing the porous surface of platinum tracks sputtered at room temperature. The image highlights the lower deposition density and poor uniformity, revealing visible surface porosity.

4.1.5 TiPt_S_50

As the platinum deposition temperature was increased, the surface structure became increasingly prominent, leading to more distinct wrinkling. In the case of platinum electrodes that were sputtered at 50°C, the periodicity of these wrinkles was consistently measured at approximately 30 μm across all samples. The width of the cracks was found to be nearly identical to those produced at room temperature.

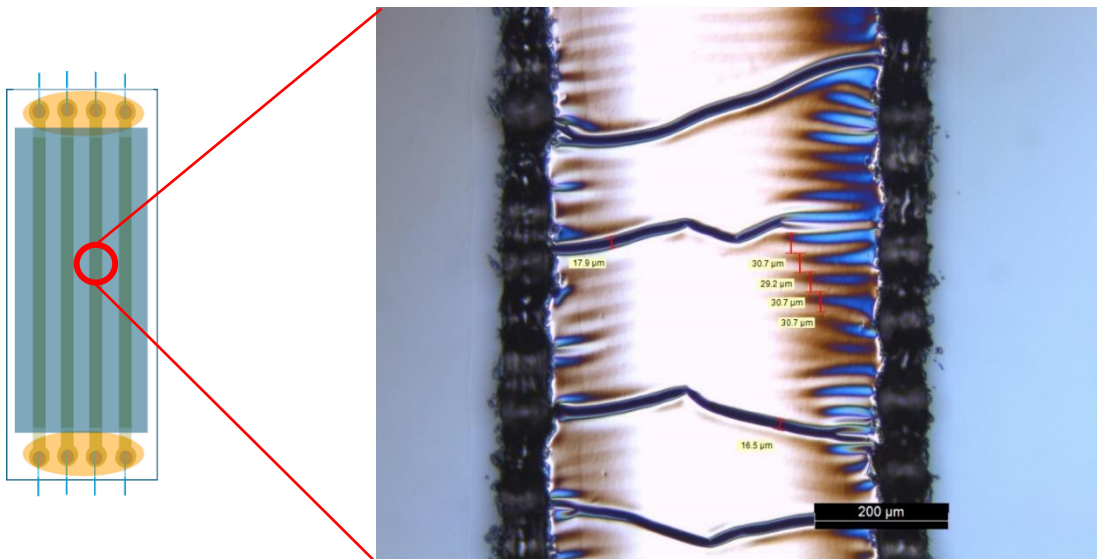


Figure 34- Microscope top view of the TiPt_S_50 sample, showing platinum tracks deposited at 50°C. The image reveals more pronounced wrinkling on the surface, with a consistent wrinkle periodicity of approximately 30 μm across all samples. The width of the cracks is similar to those observed at room temperature. Measurements of crack widths and wrinkle periodicity are also displayed.

From Figure 34, it is possible to see that these samples tend to have better uniformity and higher metallization density compared to the room-temperature sputtered ones. From Figure 34 it is still possible to see some pores, but the density was much lower as the pores were more like isolated defects rather than widespread as in the previous case.

4.1.6 TiPt_S_70

When the substrate temperature is 70°C, the tendency is for the surfaces of the samples to exhibit more pronounced wrinkles compared to those sputtered at room temperature. The samples sputtered at 70°C consistently displayed wrinkles with a higher frequency compared to the sample sputtered at 50°C, see Figure 35.

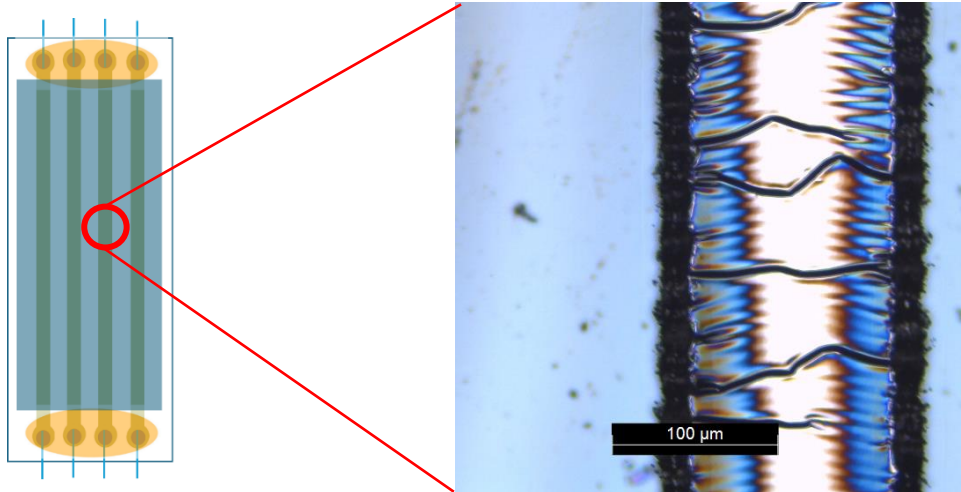


Figure 35- Microscope top view of the TiPt_S_70 sample, showing platinum tracks deposited at 70°C. The image illustrates a surface with more pronounced and frequent wrinkles compared to samples sputtered at lower temperatures.

In contrast to the approximately 30 μm wavelength of the wrinkles observed in the previous case, the wrinkles in this case have a consistent wavelength of around 17 μm across all sputtered samples, see Figure 36.



Figure 36- Microscope top view of the TiPt_S_70 sample, showing platinum tracks deposited at 70°C. The image highlights wrinkles with a consistent wavelength of approximately 17 μm. Measurements of wrinkle periodicity are displayed.

Following the optical microscopy, the 4-probe resistance measurement was carried out.

4.2 Four Probes Resistance Measurements

Following every deposition process, the sheet resistance was evaluated by conducting four-probe resistance measurements on the bridges. To ensure the accuracy of the measurements, the resistance was measured three times for each of the bridges.

To calculate the sheet resistance, we started by measuring the resistance using a four-probe method. In this setup, four probes were positioned on the bridge structure, with two probes placed on the outer pins and two on the inner pins. The multimeter, configured for four-probe measurements, supplied current through the outer probes while measuring the voltage across the inner probes. This provided the total resistance of the bridge structure. The sheet resistance was then calculated using the standard formula found in the literature [43]:

$$R_{sb} = \frac{V_{ba}}{I_{cd}} \frac{W}{L} \text{ } [\Omega/\square]$$

Equation 1: equation used to calculate the sheet resistance

Where V_{ba} is the voltage measured between points B and A, I_{cd} is the current applied between points C and D, W is the width of the conductive path, L is the length of the conductive path as shown in Figure 37, $[\Omega/\square]$ represents the sheet resistance in ohms per square.

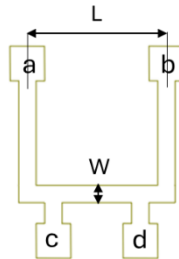


Figure 37- Bridge structure used for the four-probe measurement of sheet resistance. W represents the width of the conductive path, while L denotes the length of the conductive path.

Table 7 provides the number of samples deposited for each deposition type together with the evaluation of the sheet resistances and the mean relative deviation.

Table 7- Electrical properties of deposited films, including the number of depositions, average bridge resistance (Ω), mean relative deviation (%), and sheet resistance (Ω /square) for each sample.

Name	Number of depositions	Average Bridges (Ω)	Mean relative deviation (%)	Sheet resistance (Ω/square)
CrAu_T_Rt	8	9,390	2,1	1,9
CrAu_S_Rt	17	6,398	1,5	1,3
CrAu_S_70	15	7,097	1,7	1,4
TiPt_S_Rt	8	O.C.	0	O.C.
TiPt_S_50	15	41,900	3,1	8,4
TiPt_S_70	15	27,203	1,7	5,4

The result shows that gold samples have a comparable resistance.

The platinum tracks sputtered at room temperature lack conductivity altogether. Although some tracks exhibited a certain level of conductivity, their resistance was incredibly high in comparison to the samples that sputtered with the thermal stage, measuring in the order of k Ω . Consequently, they did not function as intended and behaved like open circuits.

On the other hand, the platinum tracks deposited at 70°C and 50°C showed conductivity, and their resistance was consistently about three times higher compared to the gold samples.

4.3 SEM Analysis

The scanning electron microscope (SEM) analysis provided a detailed view of cracks at the micrometre level. Verification of measurements obtained from the optical microscope was carried out using the SEM microscope. The SEM's capability to work with conductive materials resulted in a distinct contrast between PDMS and metal, allowing for a precise visualisation of cracks. This facilitated an accurate assessment of the crack state and the layers deposited. Unlike the optical microscope, the SEM allowed us to determine whether the cracks were deep, reaching the substrate, or superficial, preserving an intact conductive layer.

The image legend for the picture taken with the SEM Hitachi SU 8230 indicates the acceleration voltage, the working distance between the sample and the electron beam, the magnification, and the acquisition mode used in the SEM.

The image legend for the picture taken with the SEM Hitachi SU 3500 indicates the acceleration voltage, the working distance between the sample and the electron beam, the magnification, the acquisition mode used in the SEM and the chamber pressure.

4.3.1 CrAu_S_RT

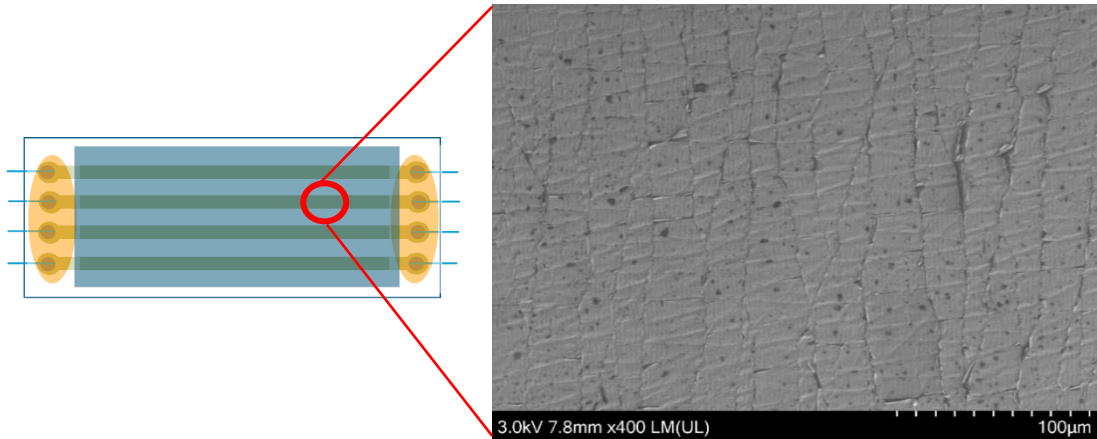


Figure 38- SEM image of a gold-sputtered sample at room temperature. Thin and large cracks are visible, forming a network along the x and y axes. The gold layer appears to peel off in larger cracks, while the underlying chromium ensures conductivity. The deposition is uniform with minor surface defects

Figure 38 displays a track of the sample sputtered with gold at room temperature. The sample was positioned horizontally inside the vacuum chamber of the SEM Hitachi SU 8230, with the track axis designated as the x-axis. To examine the sample, the secondary electron setting of the SEM was utilized with an acceleration voltage of 3 kV and a working distance of 7,8 mm between the electron beam and the sample. In this case, the mode used is LM UL (Low Magnification Upper Left).

The image reveals the presence of thin cracks along the y-axis of the sample during deposition, with larger cracks also visible. The crack pattern forms a complex network, with larger, more visible cracks along the y-axis and thinner cracks along the x-axis. Although the superficial gold layer appears to be coming off at the larger cracks, the underlying chromium remains intact, ensuring conductivity.

The image also provides insight into the uniformity of the deposition, which appears relatively consistent with diffuse surface defects rather than localized ones. Superficial holes are noticeable, but they do not penetrate deeply into the sample.

4.3.2 CrAu_S_70

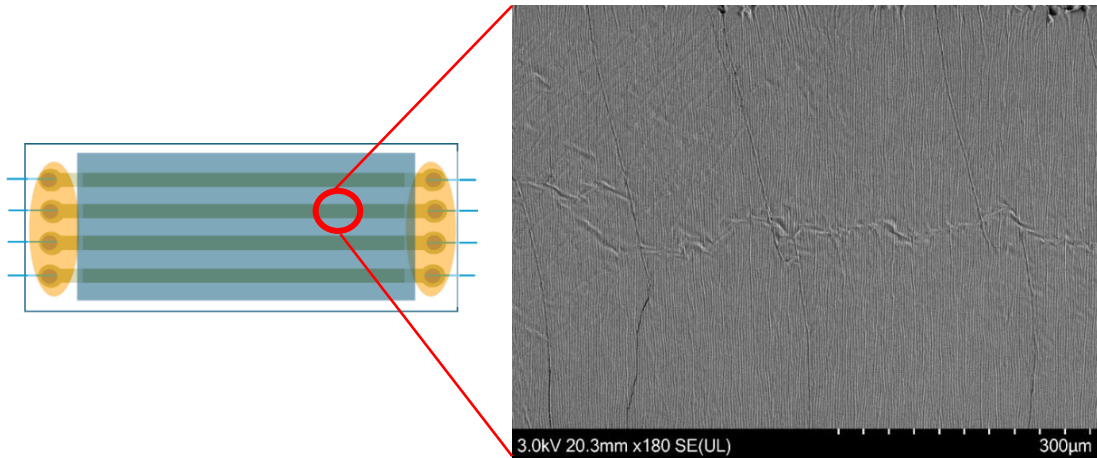


Figure 39- SEM image of the CrAu_S_70 sample sputtered at 70°C, showing an uneven, textured surface with visible wrinkles, confirming optical microscopy results.

The CrAu_S_70 sample was positioned horizontally along the x-axis inside the chamber of the SEM Hitachi SU 8230. As visible in samples that were sputtered at room temperature, even in this case the samples that sputtered at 70°C exhibited a surface that is textured, with visible wrinkles, see Figure 39. This observation aligns with the anticipated outcome derived from optical microscopy analysis.

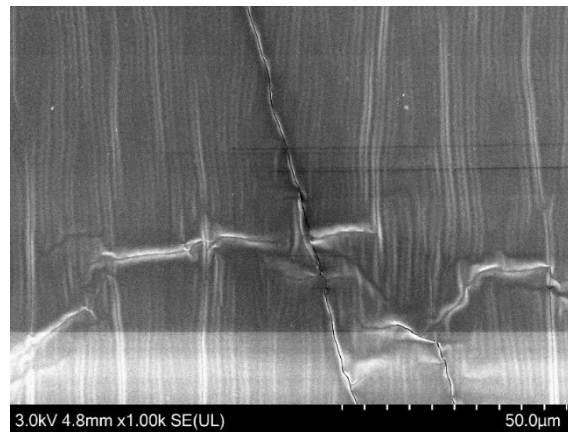


Figure 40- SEM image of the CrAu_S_70 sample sputtered at 70°C, higher magnification

The cracks in the material appear to be more prominent along the y-axis, with some superficial cracks also visible along the x-axis. Despite these cracks, the gold layer has not delaminated, indicating a thinning of the metallic layer. In addition, Figure 40 illustrates the previously discussed charging effect mentioned in 2.3 Scanning Electron Microscopy. The lighter stripe at the bottom of the image is a clear example of the charging phenomenon.

4.3.3 CrAu_T

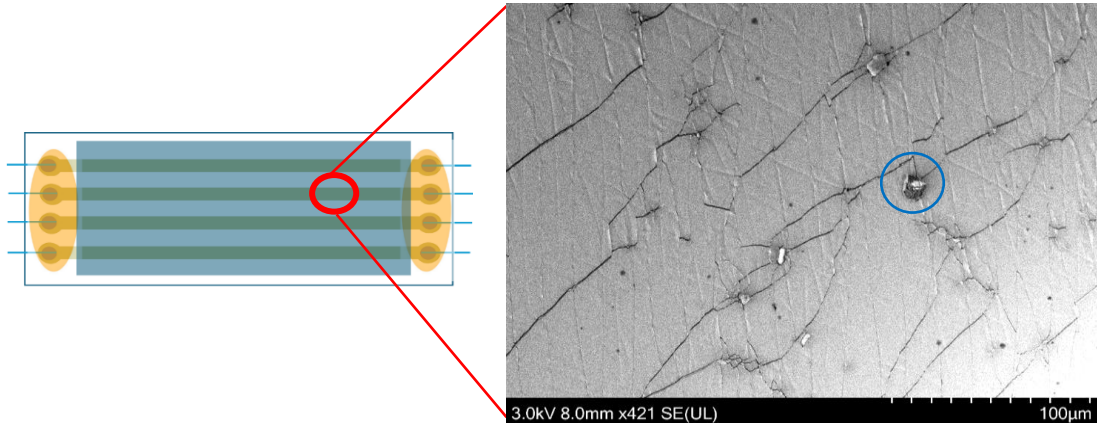


Figure 41- SEM image of CrAu_T sample thermally evaporated with gold. The image shows a non-preferential crack pattern and deeper holes, one of which, circled in red, exposes the underlying PDMS which, due to the charging effect, appears bright

The images of the CrAu_T samples were captured using the SEM Hitachi SU 8230. Figure 41 and Figure 42 illustrate the distinct patterns of samples thermally evaporated with gold.

The thermally evaporated samples display a less preferential direction of crack expansion. The image highlights a defective deposition with visually deeper holes compared to the sputtered samples. One particularly deep hole circled in blue in Figure 41, exposes the PDMS underneath, which appears bright white due to the charging effect.

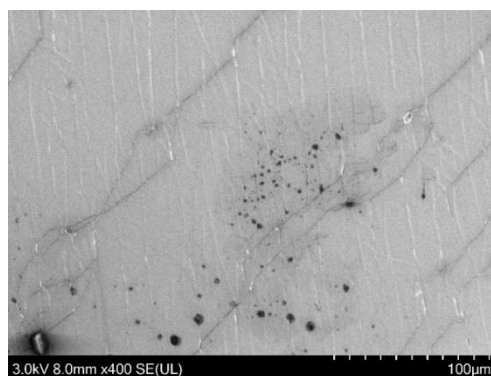


Figure 42- SEM image of CrAu_T sample, showing reduced charging effect, providing a clearer view of deep holes extending to the substrate.

Figure 42 shows less impact from the charging effect, providing a clearer view of the deep holes that propagate to the substrate and revealing poorer uniformity compared to the sputtered gold samples.

4.3.4 TiPt_S_RT

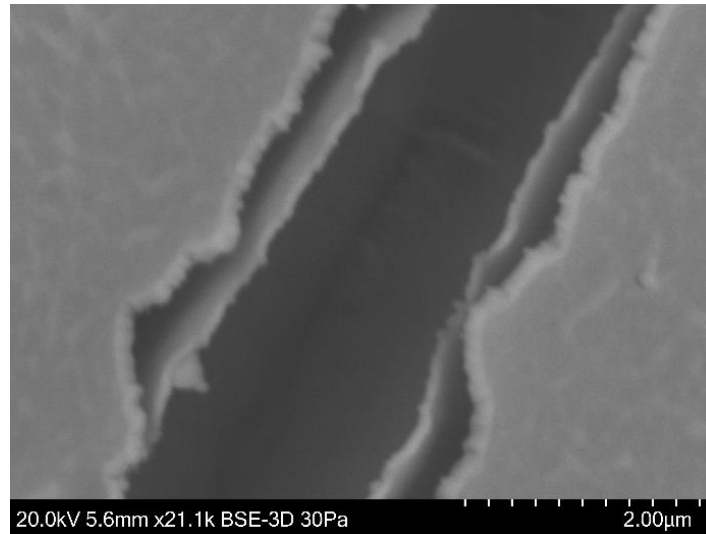


Figure 43- SEM image of TiPt_S_RT samples sputtered at room temperature. The image reveals extensive cracks affecting both the titanium and platinum layers, which expose the surface of the PDMS substrate.

The images of the TiPt_S_RT samples were captured using the SEM Hitachi SU 3500. The analysis of the platinum samples revealed that when sputtered at room temperature, the cracks were found to be extensive and had an impact on both layers, as demonstrated in the SEM image Figure 43. This observation gives us valuable information about the samples' non-conductive properties.

Figure 43 shows that both the titanium and platinum layers are exposed, revealing the surface of the PDMS. As a result, the platinum samples that sputtered at room temperature were found to be non-conductive.

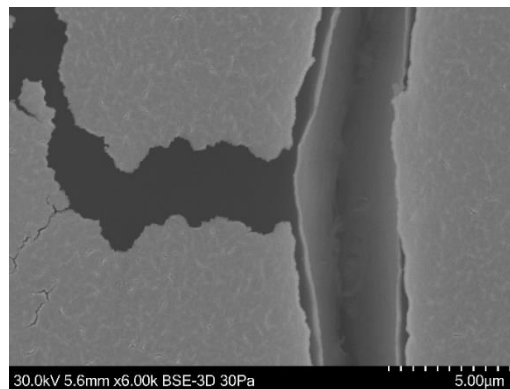


Figure 44- EM image showing the condition of TiPt_S_RT samples with ongoing conductivity despite unstable surface layers. The image highlights extensive cracking in the platinum surface layer and partial detachment of the titanium layer underneath, particularly at the edges closer to the surface.

Figure 44 shows that despite the ongoing conductivity in certain areas due to the intact layers, the situation remains highly unstable. This is evident from the cracked surface layer of platinum and the partially attached titanium layer beneath, with detachment occurring primarily at the layer's edges closer to the surface. While these cracks facilitate conductivity in the sample, they also significantly impact its mechanical properties by rendering the seemingly intact titanium layer extremely thin and fragile. Additionally, the image illustrates the presence of microcracks as seen in thermal-evaporated gold samples, which are probable contributors to the stretchability of the tracks. Fifteen cracks were examined for each sample, and all of them displayed consistent characteristics, as shown in the accompanying images.

4.3.5 TiPt_S_50

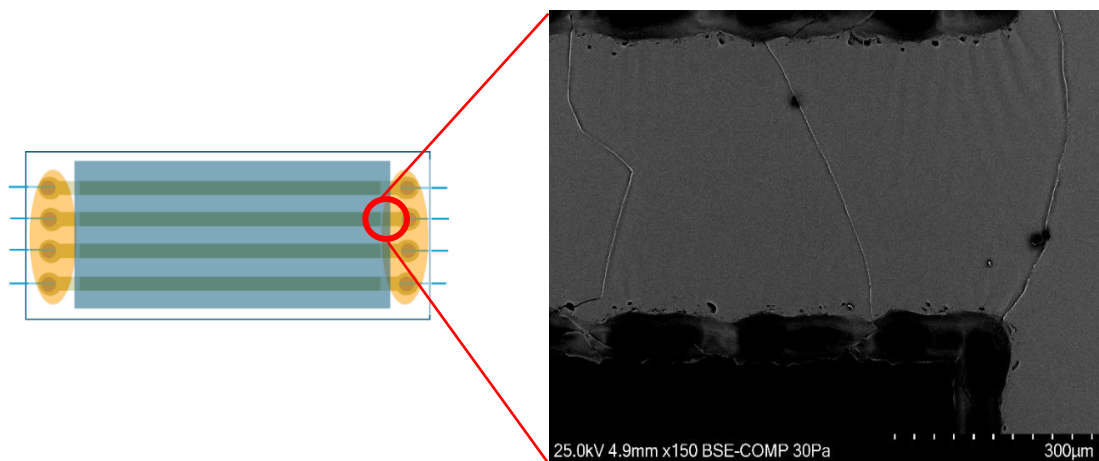


Figure 45- Top view SEM image of TiPt_S_50 samples. Compared to samples sputtered at room temperature, this image reveals a more wrinkled and homogeneous surface with fewer surface defects.

From Figure 45, it is evident that the surface, compared to samples sputtered at room temperature, is more wrinkled and more homogeneous, with fewer surface defect densities.

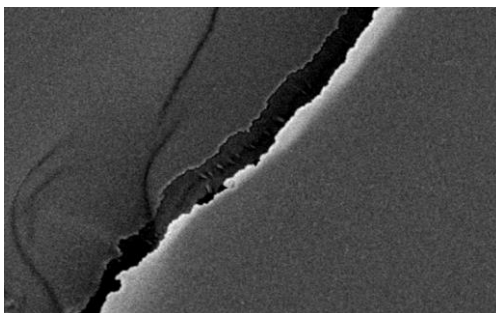


Figure 46- SEM image of TiPt_S_50 samples showing delamination of the superficial layer of platinum while the underlying titanium layer remains intact. Close-up views reveal metallic filaments at the crack location.

Figure 46 shows that only the superficial layer of platinum has delaminated, while the underlying titanium layer remains intact. Additionally, when zooming in on the image at the location of the crack, metallic filaments can be observed. These filaments likely maintain the electrical conductivity of the sample despite the presence of the crack. The analysis was conducted on fifteen cracks for each track, and the majority exhibited this structure.

4.3.6 TiPt_S_70

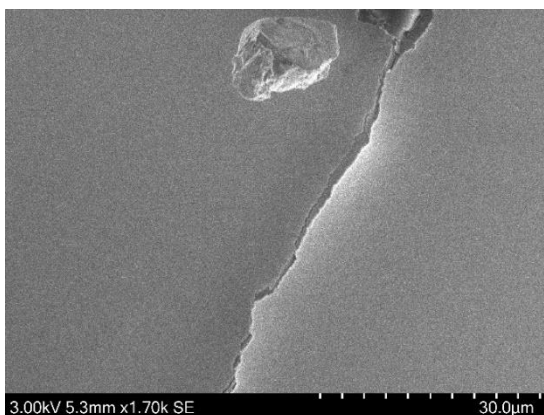


Figure 47- SEM image of TiPt_S_70 samples showing a uniform surface with minimal defects. The image reveals that only the platinum layer has detached, leaving the underlying titanium layer intact.

The SEM Hitachi SU 3500 was used to capture images of the TiPt_S_70 samples. Upon examination, the images revealed a uniform surface with minimal defects. The intact titanium layer beneath the cracks indicates that only the platinum layer has detached as shown in Figure 47. The analysis was conducted on 15 cracks for each track, and the majority exhibited this structure.

4.4 Mechanical Testing

The tables provided below outline the number of samples that have been subjected to testing for each deposition type, along with the percentage of stretching applied to each sample compared to its relaxed position. Table 8 provides an overview of the number of samples tested at two different stretching levels: 5% and 10%. For each sample type and stretching level, the table lists the count of samples that were subjected to testing

Table 8- Summary of the number of tested samples at 5% and 10% stretching levels for different deposition types.

Name of the sample	Number of Tested Samples (5% Stretching)	Number of Tested Samples (10% Stretching)
CrAu_T_Rt	0	2
CrAu_S_Rt	0	2
CrAu_S_70	2	2
TiPt_S_Rt	0	0
TiPt_S_50	2	0
TiPt_S_70	2	0

Each set of samples included four tracks, so the total number of tracks tested is four times the number of samples. Therefore, if the tables indicate that two samples were tested, this corresponds to a total of eight tracks tested.

The following graph in Figure 48 shows the results obtained for each test set, along with their respective error bars. The graph depicts the number of traction cycles on the x-axis and the corresponding increase in resistance relative to the initial resistance before the stress test on the y-axis. When referring to the legend, it follows the naming code detailed in Table 4. Specifically, when dealing with samples stretched to 5% of their original size, a dot was used as the marker. On the other hand, for samples stretched to 10% of their initial size, a triangle was used as the marker.

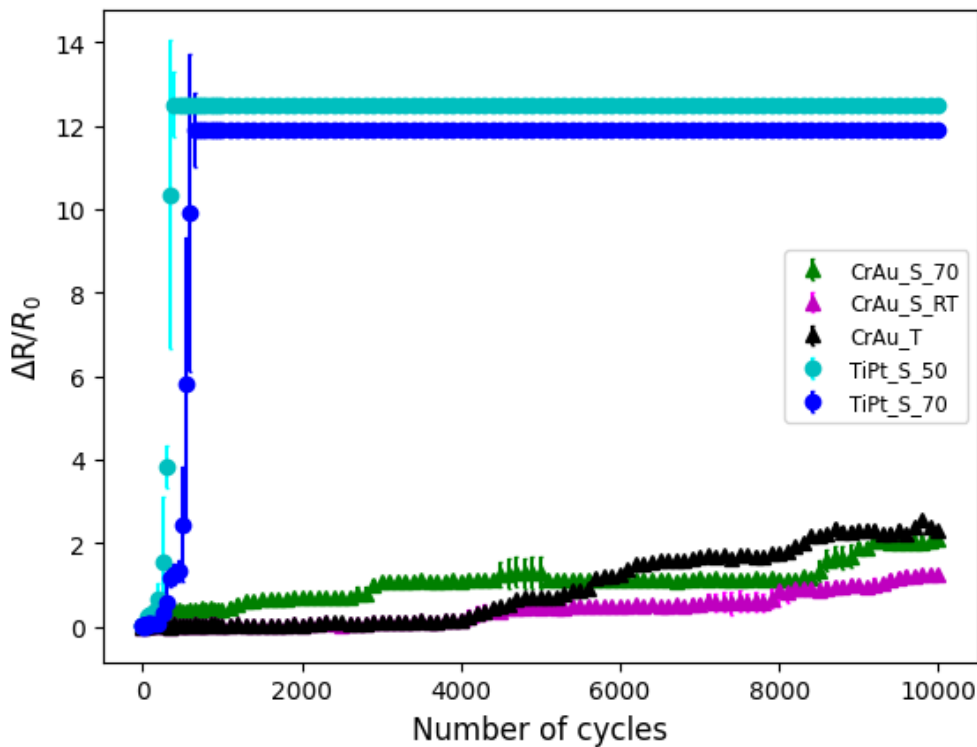


Figure 48- Graph showing the results of each test set, including error bars. The x-axis represents the number of traction cycles, while the y-axis shows the increase in resistance relative to the initial resistance before the stress test. The legend follows the naming code outlined in Table 4: samples stretched to 5% of their original size are indicated by dots, and samples stretched to 10% are represented by triangles.

The findings show that the platinum samples failed after significantly fewer cycles compared to the gold samples. Specifically, the platinum samples sputtered at 50°C failed after 400 tensile cycles, while those sputtered at 70°C failed after 600 cycles. Beyond this point, the resistance of the tracks increased to infinity, indicating an open circuit. It is also noted that as the measured resistance increases, the error bars become significantly larger. For visualization purposes, the graph has an upper resistance limit set, but this represents an open circuit.

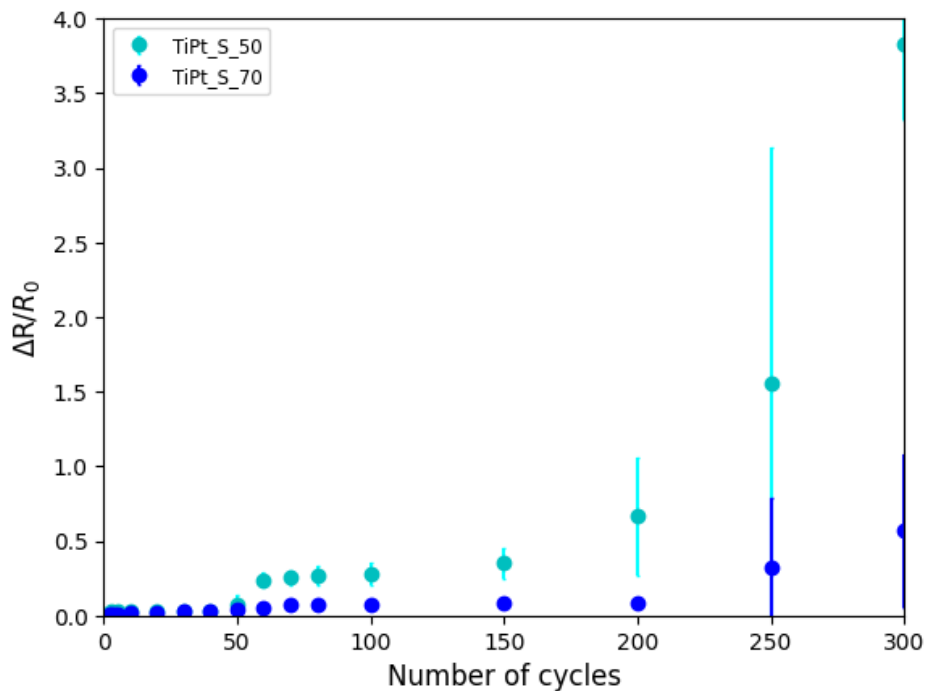


Figure 49- Graph focusing solely on the platinum samples, with both the x-axis and y-axis adjusted for improved visualization. The x-axis represents the number of tensile cycles, while the y-axis shows the increase in resistance relative to the initial resistance before the stress test.

To focus on the platinum samples, gold tracks have been removed from the graph, and both the x-axis and y-axis have been truncated. Figure 49 illustrates that the relative resistances of the platinum tracks increase very rapidly, with a profile that appears more parabolic than linear. This suggests a rapid acceleration in resistance as the tensile cycles progress, rather than a steady, linear increase.

In contrast, all gold samples endured up to a total of 10,000 tensile cycles. Although 10,000 cycles is the maximum point to which the samples were visualized, they still maintained very good resistance at this stage. The increase in resistance relative to the initial value was notably lower compared to the platinum samples, demonstrating that the gold samples performed significantly better under tensile cycles.

To focus more closely on the gold samples, the graph has been recreated without including the platinum samples, see Figure 50. This adjustment allows for a reduced y-axis range, facilitating a clearer observation of the differences in behaviour among the gold samples sputtered with various deposition techniques and parameters. The data in the graph in Figure 50 indicates that the tracks sputtered at room temperature demonstrate the highest performance. Specifically, the gold samples sputtered at

room temperature exhibit the lowest increase in relative resistance after 10,000 tensile cycles, showing superior durability compared to those sputtered at 70°C and those deposited using thermal evaporation.

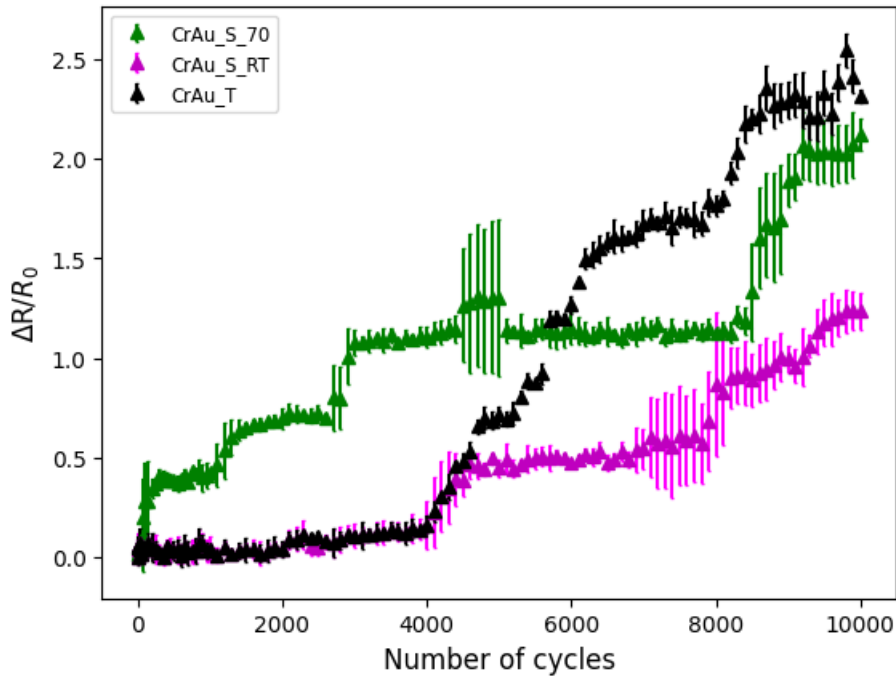


Figure 50- Graph focusing exclusively on the gold samples, with platinum samples excluded. The x-axis represents the number of tensile cycles, while the y-axis shows the increase in resistance relative to the initial resistance before the stress test.

The CrAu_S_70_10 samples exhibit a mostly linear increase in resistance values, with occasional step-like increments. Notably, between the 4000th and 6000th cycles, the error bars widen significantly, indicating variability in resistance increase among the samples during this period. This suggests that not all samples experienced the same rate of resistance increase simultaneously.

Similarly, the CrAu_S_RT samples also display occasional step-like increments in resistance. As the number of cycles approaches 10,000, the error bars tend to increase, suggesting growing variability in resistance measurements among the samples.

In contrast, the CrAu_T samples exhibit more pronounced step-like behaviour. The resistance increase for these samples is characterized by nearly flat periods interrupted by higher, flat resistance values, creating a clear step-like pattern. The

samples subjected to thermal deposition show the smallest error bars, indicating more consistent performance compared to the sputtered.

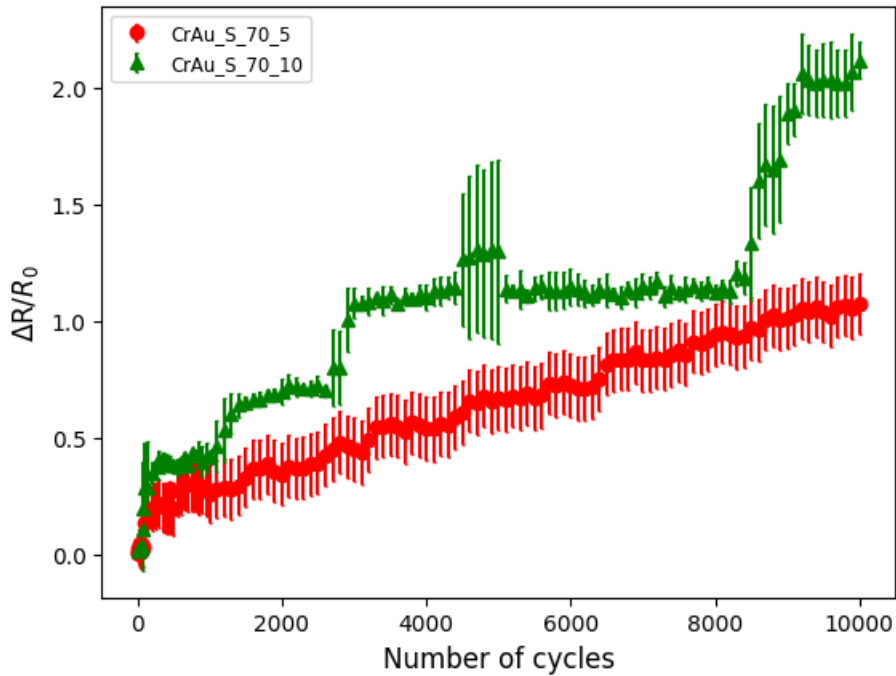


Figure 51- . Graph showing the results for CrAu_S_70 samples sputtered at 70°C, tested with 5% and 10% stretching levels. The x-axis represents the number of traction cycles, and the y-axis indicates the increase in resistance relative to the initial resistance before the stress test. Samples stretched to 5% are marked with dots, while samples stretched to 10% are marked with triangles.

Additionally, the CrAu_S_70 samples were tested at both 5% and 10% stretching levels, further demonstrating a dependency on the stretching percentage. The results are reflected in the CrAu_S_70_5 and CrAu_S_70_10 curves, which illustrate the differences in resistance behaviour. The CrAu_S_70_5 curve shows a progressively linear increase in resistance without the distinct step-like increments observed in the CrAu_S_70_10 curve. These variations highlight how different stretching levels affect the performance of the samples, as shown in Figure 51.

5 Discussion

The primary innovation of this project lies in the investigation of the stretchability of conductive tracks. Specifically, for gold, this research explores stretchability on samples produced via sputtering, whereas it is typically conducted using thermal deposition. Additionally, another significant innovation is the analysis of stretchability for platinum tracks, which is less commonly studied. As previously mentioned, existing implantable electrodes are either rigid or flexible. However, neither rigidity nor flexibility inherently supports stretchability.

The comparison of platinum and gold deposition in terms of stretchability underscores the complexity of material selection and explains why platinum has been less explored for stretchable applications. While platinum is preferred in the biomedical field due to its chemical properties—discussed in 2.6.2 Platinum—that negate the need for encapsulation, it is less utilized when stretchability is a key requirement. Our research group is currently focused on the encapsulation of gold electrodes, which necessitates this additional step. The process is challenging and involves using PEDOT-PSS, a conductive polymer synthesized in-house, and developing a protocol for electropolymerizing PEDOT onto PDMS-Au electrodes. In contrast, platinum's biochemical properties offer the potential to bypass encapsulation altogether. This makes platinum particularly appealing for our research, as encapsulation remains one of the most complex steps in fabricating stretchable gold-based devices.

Platinum samples were produced using the sputtering technique because it is a refractory metal that does not easily reach the high temperatures required for thermal evaporation [29]. As a result, platinum was not deposited via thermal evaporation, and even with sputtering, the deposition rate was found to be very low compared to the gold one.

Platinum samples were deposited using sputtering at three different temperatures: room temperature, 50°C, and 70°C. These temperature points were selected based on their relevance to the stability of the PDMS substrate and practical considerations in the deposition process. Specifically, 70°C was chosen as it approaches the degradation threshold for PDMS, representing an upper limit for maintaining the material's optimal properties. On the other hand, 50°C was selected due to prior

observations with gold deposition via thermal evaporation, where the temperature gauge indicated that the temperature never reached 70°C, with actual measurements from previous studies by our research team showing that the maximum temperature within the deposition chamber was around 50°C. For the gold samples, sputtering was conducted at room temperature and 70°C for similar reasons. Room temperature was used as a baseline, while 70°C was chosen to explore the upper limit of the process and to assess the impact on the material properties, given its proximity to the degradation threshold of the PDMS substrate.

Based on the previous research findings from our group, it was established that gold samples could withstand stretching up to 10% strain. Therefore, stretching tests for the gold samples were initiated at this 10% strain level, which allowed us to evaluate their performance under maximum expected deformation. In contrast, due to the absence of prior data on the stretchability of platinum samples, a more conservative approach was adopted. Without established benchmarks for platinum under similar conditions, stretching tests began at a lower strain level of 5%. This cautious approach was employed to carefully assess the initial performance and behaviour of the platinum samples. By starting at a reduced strain level, we aimed to prevent potential damage or failure of the platinum tracks during the preliminary testing phase.

Upon reviewing the results presented in the previous section and comparing them with results obtained by the researcher I worked with, who conducted similar tests on gold devices with thermal evaporation (which have not yet been published, and thus specific numerical data cannot be shared), it is evident that the outcomes of this project demonstrate superior performance in terms of resistance increase with the number of stretching cycles.

However, it is important to note that the colleague's results showed a resistance increase approximately double the ones observed in this research after 10,000 cycles. This discrepancy arises because the devices in our project did not include interconnections. The creation of these interconnections posed significant technical challenges, as the available technologies and tools were more compatible with rigid substrates, while our work involved a highly delicate and flexible substrate. Due to time constraints and the need to proceed with mechanical testing, further research on encapsulation was not conducted, leading to the use of manual measurements. Although the tracks initially appeared conductive after the interconnection process, they lost conductivity when the samples were removed from the petri dish and placed

on the support for mechanical testing. This indicated weak interconnections, resulting in nonfunctional devices. Microscopic examination revealed that the conductive paste used was too rigid for the tracks, creating a mechanical mismatch. This issue led to the tracks breaking and developing deep cracks along the interface between the deposition and the conductive paste application point, as shown in Figure 52. Attempts to use a more flexible paste were unsuccessful in addressing this problem.

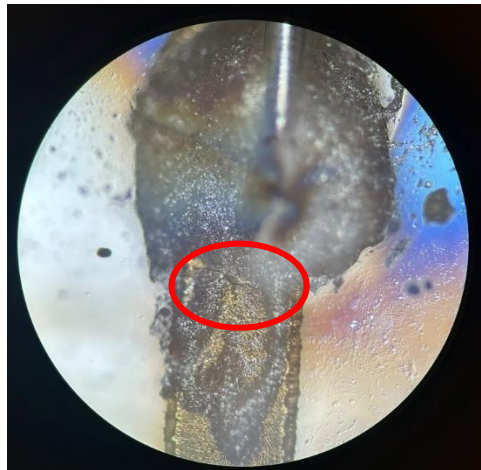


Figure 52- Optical microscope image of a track with silver conductive paste applied. The area circled in red highlights a crack at the interface between the conductive paste and the track, which led to the tracks becoming non-conductive.

Furthermore, the “neck” of the sample, being more fragile and susceptible to mechanical stress compared to the track itself, might have contributed to the issue. Applying the conductive paste specifically to this part might have mitigated the problem, but this potential solution was not tested due to time constraints, leaving its effectiveness unknown.

The mechanical test data were influenced by several factors related to the measurement process. Specifically, resistance measurements were taken from the circular sections of the track, shown in Figure 53, which provides a visual representation of the track design with measurement points highlighted in red. Given the extreme thinness of the deposited layers, a rounded needle was used to perform these resistance measurements. However, despite this careful approach, the measurement points experienced progressive damage with each test cycle.



Figure 53- Design of the track with resistance measurement locations indicated in red. The figure shows the circular parts of the track where measurements were conducted.

The issue of damage was exacerbated by the fact that the safety margin left during encapsulation was utilized to take measurements on non-encapsulated sections once the primary measurement points became too damaged. This situation introduced potential errors into the data. When the measurement points became too worn or compromised, the resistance measured might reflect areas of the track that were not initially intended for measurement. Consequently, this can lead to an overestimation of the samples' tensile resistance. This overestimation occurs because a shorter track length used for resistance measurement is typically associated with lower resistance readings. Therefore, when measurement points that are damaged or no longer functional are replaced by non-encapsulated sections, the recorded resistance values may not accurately represent the performance of the sample as initially tested. This discrepancy between the initial and subsequent measurement setups results in variability and potential inaccuracies in the reported stretching resistance of the tracks. Conversely, the same interconnection problems might have led to an underestimation of tensile resistance in the colleague's research. Since it is unclear whether the increase in resistance observed by the colleague was due to the tracks themselves or the interconnections, this uncertainty complicates the comparison of results. Therefore, the impact of interconnections remains a significant factor in interpreting resistance data and highlights the need for careful consideration of these variables in future studies. Many research groups are grappling with similar challenges, as creating stable and effective interconnections for thin, flexible devices proves to be particularly difficult.

A thorough review of the scientific literature on metal deposition on flexible substrates has identified two key factors that most significantly influence a material's resistance to tensile stress: the formation of microcracks and the surface structure of the metal layer. The results of the tensile stress tests were presented in the previous section. However, when interpreting these results, it is important to consider that the devices were mounted onto the support of the test setup with great care to ensure the surface was flat and not pre-stretched before testing. Despite this, a system to guarantee

completely non-prestretched or perfectly flat positioning of the tracks was not implemented.

Furthermore, the different tracks on the devices may have experienced varying degrees of stress depending on their position and how the PDMS deformed. As a result, the outermost tracks could have been subjected to different mechanical stresses compared to those located internally.

The results shown in Figure 49 display a trend that seems to support the literature hypothesis. Specifically, when comparing the platinum tracks, the ones sputtered at 70°C demonstrated better performance compared to those sputtered at 50°C.

Microscope images of the platinum tracks reveal that those deposited at higher temperatures exhibit a more wrinkled surface. However, in terms of microcracks, both sets of samples show no significant differences, either in size or distribution.

The analysis of the platinum tracks also mentions tracks sputtered at room temperature, which, as previously noted, were non-conductive immediately after deposition and had much flatter surfaces compared to the thermally treated samples. Additionally, the performance in terms of stretchability improves as the surface wrinkling increases. Based on the results obtained, it appears that the degree of wrinkling depends on the deposition temperature. This can be explained by considering the difference in the coefficients of thermal expansion (CTEs) between the Sylgard polymer substrate and the metallic depositions.

During the sputtering process, the sample was mounted on the support wafer inside the reaction chamber and secured with Kapton tape on all four sides. The heat applied by the thermal stage likely caused the device to expand during deposition. It's important to note that polymers, such as PDMS, typically have a much higher CTE, meaning they expand significantly when exposed to heat, whereas metals tend to have CTE values roughly 20 times lower and are much less affected by temperature changes. Once the deposition was complete and the device was removed from the heated chamber and cooled back to room temperature, the PDMS contracted, pulling the deposited metal along with it, thereby creating the wrinkled surface observed under the microscope.

When comparing gold samples, Figure 50 shows that in terms of stretchability after 10,000 cycles, the gold devices sputtered at room temperature performed the best,

followed by the gold tracks sputtered at 50°C, and lastly, those obtained through thermal deposition. This indicates that the sputtering technique outperforms thermal deposition in terms of performance.

“Thermal evaporation is the most employed technique for the deposition of these samples mainly because it can provide films of extreme purity and known structure. For example, in electrochemical sensors, where the electrocatalytic activity of the top monolayers of the sensing electrode determines proper operation, material purity is a priority consideration. However, sputtering is renowned for providing excellent adhesion between the substrate and the film, minimal shadowing effect, and control over the deposited film's characteristics through adjustments in bias, pressure, and substrate heating. Because the sputtering target is much larger compared to an evaporation point source, shadowing is significantly reduced” [29].

Looking at the optical microscope and SEM images, the most notable difference between the gold samples is the presence of numerous surface defects in the tracks produced via thermal deposition, whereas the sputtered gold tracks exhibit a more uniform deposition with fewer surface defects.

In terms of crack width, there is no significant difference between the thermal evaporated and sputtered samples. However, a distinction is observed in the pattern and organization of the cracks. For thermally evaporated samples, the cracks tend to form a more complex and intricate network compared to the relatively simpler pattern seen in the sputtered samples. This variation in crack formation may be influenced by the differences in temperature management between the two deposition techniques. In thermal deposition, the increase in temperature is the mean thanks to which the deposition occurs. During thermal evaporation, the chamber is heated throughout the deposition process to guarantee the evaporation and subsequent condensation of the material onto the substrate.

Conversely, in sputtering, the chamber is preheated before the deposition process begins. The temperature does not fluctuate as significantly during deposition as it does in thermal evaporation.

The manner in which atoms are accelerated and deposited onto the substrate in sputtering, with a more controlled thermal environment, may contribute to the formation of a simpler crack network compared to the more dynamic thermal conditions of evaporation.

In theory, the denser network of microcracks present in the tracks produced via thermal evaporation should, according to bibliographic hypotheses, enhance stretchability. This is based on the idea that microcracks act like springs: they open under tension and close to restore contact when the material relaxes, thus potentially improving tensile resistance. However, the actual results observed in this research indicate the opposite. Despite the expected benefits of a complex microcrack network, the thermal evaporation tracks did not outperform the sputtered tracks in terms of stretchability.

Compared to gold tracks deposited via thermal evaporation, the gold-sputtered tracks exhibit significantly less flat surfaces and more pronounced wrinkling. This wrinkling may have potentially enhanced stretchability, as the wrinkles may help distribute accumulated stresses during mechanical tensile loading, potentially leading to better performance under stretch.

When comparing the results of gold tracks with those of platinum, an interesting reversal in the effect of the sputtering temperature on stretchability is observed. For platinum samples, increasing the sputtering temperature from room temperature (RT) to 50°C and 70°C actually extends their stretchability. In contrast, for gold tracks, higher temperatures led to reduced stretchability. In the case of platinum, the specimens sputtered at 50°C and 70°C exhibited a much more wrinkled surface compared to those sputtered at RT. This difference is evident from optical microscope and SEM images, which show a more pronounced wrinkling effect at higher temperatures for platinum samples compared to the gold samples. This significant increase in wrinkling in platinum, compared to the gold samples, may account for the observed reversal in trends.

In the gold tracks' case, despite not observing significant differences in the wrinkling of the surface or the width and arrangement of cracks, while changing the sputtering temperature, the theoretical framework provides insights into the underlying mechanisms.

Theory suggests that at low sputtering temperatures, surface diffusion—the process by which adsorbed atoms or molecules move across the surface—is slower compared to the rate at which film precursors arrive. When the temperature is low, the precursor molecules that arrive at the surface are more likely to interact with each other before they have a chance to diffuse and spread out. This interaction can lead to the formation of an amorphous film, which lacks a well-ordered structure but possesses

inherent slip planes along which atoms can move. On the other hand, at high temperatures, surface diffusion is much faster relative to the incoming flux of precursor molecules. In such conditions, adsorbed species can move more readily across the surface, allowing them to reach and form bonds at step growth sites [29]. This process promotes the formation of single-crystal materials, which typically have a more ordered and regular atomic arrangement. The difference in surface diffusion rates between low and high temperatures explains why amorphous films, which are more common at lower temperatures, might exhibit greater resistance to stress cycles. The lack of a well-defined structure in amorphous films, combined with the presence of slip planes, allows for some movement and adjustment of atoms under stress. This flexibility can enhance the material's ability to withstand repeated mechanical loading and deformation.

In light of these findings, it is evident that although theoretical models predict that a denser network of microcracks and increased surface wrinkling could improve stretchability, the experimental results reveal a more intricate relationship between deposition methods, material properties, and mechanical performance. The varying performance between gold and platinum, especially concerning sputtering temperature, underscores the complex behaviour of materials under tensile stress and emphasizes the necessity for a more thorough exploration of the underlying mechanisms.

6 Conclusion

This study has suggested that sputtered gold samples might outperform those produced by thermal evaporation in terms of stretchability. The observed improvement in sputtered gold could indicate its potential for more reliable and durable applications across various industries. However, these findings should be interpreted with caution, and further investigation is necessary to confirm these potential advantages.

Additionally, the study highlights that our research is still in its preliminary stages, building on previous work by our university colleagues who focused on optimizing parameters for gold thermal evaporation. Given the limited number of tested samples and the preliminary nature of this research, drawing definitive conclusions or developing a robust theory might be premature. The current findings suggest promising trends but require more extensive studies to establish solid theories.

The current focus on platinum, despite its potential benefits, remains relatively underexplored within the scientific community. This gap indicates that further research could be valuable. Although challenges were encountered with platinum samples, it is important not to dismiss their potential. Preliminary results suggest that temperature may have a significant impact on their stretchability. In this study, the sputtering temperature was maintained at a constant level. However, exploring the effects of a linearly increasing temperature—similar to the thermal conditions in thermal evaporation—might provide additional insights into platinum's performance.

Furthermore, while temperature was a primary variable in this study, other factors may also influence material properties and performance. Parameters such as the thickness of the deposition layer, chamber pressure, and other deposition conditions could potentially affect the results. Investigating these variables in future research might offer a deeper understanding of how to optimize deposition techniques and enhance material durability.

The observations made regarding gold samples are currently limited to a stretching cycle range of up to 10,000 cycles. Beyond this range, it remains unclear how the

performance of these samples might evolve. There could potentially be an exponential increase in resistance or a plateau effect. Future studies could explore these aspects further to gain a more comprehensive understanding of the long-term behaviour of these materials under continuous stretching.

Additionally, it might have been insightful to examine how resistance changes while the samples are in a stretched state. Resistance measurements were conducted when the devices were in their relaxed position after stretching, which may not fully capture the material's behaviour under tension. Analyzing resistance in the stretched condition could have provided valuable information on whether cracks act like rigid springs, potentially influencing overall material performance. Unfortunately, due to the failure of interconnections, which hindered the automation of resistance measurements, this aspect could not be fully explored. Manual measurements were used, which may have limited the ability to systematically assess resistance variations during stretching and understand the dynamic behaviour of cracks under tensile stress. Future research could benefit from developing more reliable interconnection techniques and automated measurement systems to address these issues.

In summary, while sputtered gold has demonstrated potentially superior resilience under stretching conditions compared to thermal evaporation, the challenges with platinum underscore the complexity of material behaviour across different fabrication methods and environmental conditions. Given the limited sample size and preliminary nature of this study, future research should not only vary temperature but also systematically investigate other factors such as deposition thickness and chamber pressure. Addressing these aspects, along with improving interconnection methodologies, could be crucial for fully understanding and leveraging the potential benefits of these materials. Such comprehensive studies might lead to significant innovations and advancements in technological applications.

References/bibliography

- [1] J. Park *et al.*, «Electromechanical cardioplasty using a wrapped elasto-conductive epicardial mesh», *Sci Transl Med*, vol. 8, fasc. 344, p. 344ra86, giu. 2016, doi: 10.1126/scitranslmed.aad8568.
- [2] D. Khodagholy *et al.*, «NeuroGrid: Recording action potentials from the surface of the brain», *Nat. Neurosci.*, vol. 18, dic. 2014, doi: 10.1038/nn.3905.
- [3] R. Chen, A. Canales, e P. Anikeeva, «Neural recording and modulation technologies», *Nat. Rev. Mater.*, vol. 2, fasc. 2, p. 16093, gen. 2017, doi: 10.1038/natrevmats.2016.93.
- [4] A. F. Renz, A. M. Reichmuth, F. Stauffer, G. Thompson-Steckel, e J. Vörös, «A guide towards long-term functional electrodes interfacing neuronal tissue», *J. Neural Eng.*, vol. 15, fasc. 6, p. 061001, ott. 2018, doi: 10.1088/1741-2552/aae0c2.
- [5] S.-K. Kang *et al.*, «Bioresorbable silicon electronic sensors for the brain», *Nature*, vol. 530, fasc. 7588, pp. 71–76, feb. 2016, doi: 10.1038/nature16492.
- [6] M. K. Lyons, «Deep Brain Stimulation: Current and Future Clinical Applications», *Mayo Clin. Proc.*, vol. 86, fasc. 7, pp. 662–672, lug. 2011, doi: 10.4065/mcp.2011.0045.
- [7] G. D'Haens *et al.*, «Neuroimmune Modulation Through Vagus Nerve Stimulation Reduces Inflammatory Activity in Crohn's Disease Patients: A Prospective Open-label Study», *J. Crohns Colitis*, vol. 17, fasc. 12, pp. 1897–1909, dic. 2023, doi: 10.1093/ecco-jcc/jjad151.
- [8] F. Venail *et al.*, «Reliability and Complications of 500 Consecutive Cochlear Implantations», *Arch. Otolaryngol. Neck Surg.*, vol. 134, fasc. 12, pp. 1276–1281, dic. 2008, doi: 10.1001/archoto.2008.504.
- [9] E. M. Maynard, C. T. Nordhausen, e R. A. Normann, «The Utah Intracortical Electrode Array: A recording structure for potential brain-computer interfaces», *Electroencephalogr. Clin. Neurophysiol.*, vol. 102, fasc. 3, pp. 228–239, mar. 1997, doi: 10.1016/S0013-4694(96)95176-0.
- [10] L. A. Geddes, «Historical highlights in cardiac pacing», *IEEE Eng. Med. Biol. Mag.*, vol. 9, fasc. 2, pp. 12–18, giu. 1990, doi: 10.1109/51.57859.

- [11] S. Lacour, G. Courtine, e J. Guck, «Materials and technologies for soft implantable neuroprostheses», *Nat. Rev. Mater.*, vol. 1, set. 2016, doi: 10.1038/natrevmats.2016.63.
- [12] G. Hong, R. D. Viveros, T. J. Zwang, X. Yang, e C. M. Lieber, «Tissue-like Neural Probes for Understanding and Modulating the Brain», *Biochemistry*, vol. 57, fasc. 27, pp. 3995–4004, lug. 2018, doi: 10.1021/acs.biochem.8b00122.
- [13] Muhammad Hassan *et al.*, «Significance of Flexible Substrates for Wearable and Implantable Devices: Recent Advances and Perspectives», *Adv. Mater. Technol.*, vol. 7, fasc. 3, nov. 2021, [Online]. Disponibile su: <https://doi.org/10.1002/admt.202100773>
- [14] Sigurd Wagner *et al.*, «Electronic skin: architecture and components», *Phys. E Low-Dimens. Syst. Nanostructures*, vol. 25, fasc. Issues 2–3, p. Pages 326-334, 2004.
- [15] I. Minev, N. Wenger, G. Courtine, e S. Lacour, «Research Update: Platinum-elastomer mesocomposite as neural electrode coating», *APL Mater.*, vol. 3, p. 014701, gen. 2015, doi: 10.1063/1.4906502.
- [16] F.-T. Zhang *et al.*, «Electroless Deposition Metals on Poly(dimethylsiloxane) with Strong Adhesion As Flexible and Stretchable Conductive Materials», *ACS Appl. Mater. Interfaces*, vol. 10, fasc. 2, pp. 2075–2082, gen. 2018, doi: 10.1021/acsami.7b15726.
- [17] S. P. Lacour, S. Wagner, Z. Huang, e Z. Suo, «Stretchable gold conductors on elastomeric substrates», *Appl. Phys. Lett.*, vol. 82, fasc. 15, pp. 2404–2406, 2003, doi: 10.1063/1.1565683.
- [18] J. Jones, S. Lacour, S. Wagner, e Z. Suo, «Stretchable wavy metal interconnects», *J. Vac. Sci. Technol. Vac. Surf. Films*, vol. 22, pp. 1723–1725, ago. 2004, doi: 10.1116/1.1756879.
- [19] I. M. Graz, D. P. J. Cotton, e S. P. Lacour, «Extended cyclic uniaxial loading of stretchable gold thin-films on elastomeric substrates», *Appl. Phys. Lett.*, vol. 94, fasc. 7, p. 071902, feb. 2009, doi: 10.1063/1.3076103.
- [20] T. Adrega e S. Lacour, «Stretchable gold conductors embedded in PDMS and patterned by photolithography: Fabrication and electromechanical characterization», *J. Micromechanics Microengineering*, vol. 20, p. 055025, apr. 2010, doi: 10.1088/0960-1317/20/5/055025.
- [21] J. Zhu, X. Wu, J. Jan, S. Du, J. Evans, e A. C. Arias, «Tuning Strain Sensor Performance via Programmed Thin-Film Crack Evolution», *ACS Appl. Mater.*

- Interfaces*, vol. 13, fasc. 32, pp. 38105–38113, ago. 2021, doi: 10.1021/acsami.1c10975.
- [22] S. W. Kim, S. Lee, D. Kim, S. G. Lee, e K. Cho, «Omnidirectionally Stretchable Metal Films with Preformed Radial Nanocracks for Soft Electronics», *ACS Appl. Nano Mater.*, vol. 3, fasc. 7, pp. 7192–7200, lug. 2020, doi: 10.1021/acsanm.0c01536.
- [23] S. Yu, L. Ma, J. Zhang, L. He, e Y. Ni, «Localization of wrinkle patterns by crack-tip induced plasticity: Experiments and simulations», *Int. J. Solids Struct.*, vol. 178–179, pp. 108–119, dic. 2019, doi: 10.1016/j.ijsolstr.2019.06.004.
- [24] C. F. Guo *et al.*, «Fatigue-free, superstretchable, transparent, and biocompatible metal electrodes», *Proc Natl Acad Sci U A*, vol. 112, fasc. 40, pp. 12332–12337, ott. 2015, doi: 10.1073/pnas.1516873112.
- [25] G. Schiavone *et al.*, «Soft, Implantable Bioelectronic Interfaces for Translational Research», *Adv. Mater.*, vol. 32, p. 1906512, mar. 2020, doi: 10.1002/adma.201906512.
- [26] V. Paggi *et al.*, «A soft, scalable and adaptable multi-contact cuff electrode for targeted peripheral nerve modulation», *Bioelectron. Med.*, vol. 10, p. 6, feb. 2024, doi: 10.1186/s42234-023-00137-y.
- [27] Sami Franssila, *Introduction to Micro Fabrication*. John Wiley & Sons, Ltd, 2004.
- [28] Tai-Ran Hsu, *MEMS and Microsystems*, Second. New Jersey: John Wiley & Sons, 2008.
- [29] M. J. Madou, *Fundamentals of microfabrication and nanotechnology. Volume II, Manufacturing techniques for microfabrication and nanotechnology*, 3rd ed. Boca Raton, FL: CRC Press, 2012.
- [30] Yang Leng, *Materials Characterization*, Second. Wiley-VCH, Weinheim, 2013.
- [31] K. Norrman, A. Ghanbari-Siahkali, e N. B. Larsen, «6 Studies of spin-coated polymer films», *Annu. Rep. Sect. C Phys. Chem.*, vol. 101, fasc. 0, pp. 174–201, 2005, doi: 10.1039/B408857N.
- [32] M. Tyona, «A theoretical study on spin coating technique», *Adv. Mater. Res.*, vol. 2, dic. 2013, doi: 10.12989/amr.2013.2.4.195.
- [33] S. L. Hellstrom, «Basic Models of Spin Coating», ott. 2007.
- [34] Meyerhofer, «Key stages in spin coating process», *J Appl. Phys*, vol. 49, fasc. 3993, 1978.
- [35] Hanaor, D., Trianni, G. and Sorrell, C. (2011), “Morphology and photocatalytic activity of highly oriented e Hanaor, D., Trianni, G. and Sorrell, C., «Morphology

- and photocatalytic activity of highly oriented mixed phase titanium dioxide thin film», *Surf. Coat. Tech.*, pp. 855–874, 2011.
- [36] Yogesh B. Gianchandani, Osamu Tabata, e Hans Zappe, *Comprehensive Microsystems*, vol. 1, 3 voll. Elsevier B.V., 2008.
- [37] Michael A. Brook, *Silicon in Organic, Organometallic and Polymer Chemistry*. New York: John Wiley & Sons, 2000.
- [38] Q. Liu, R. Li, e T. Fang, «Investigating and modeling PET methanolysis under supercritical conditions by response surface methodology approach», *Chem. Eng. J.*, vol. 270, pp. 535–541, giu. 2015, doi: 10.1016/j.cej.2015.02.039.
- [39] G. C. Bond, C. Louis, e D. T. Thompson, *Catalysis by Gold*, vol. Volume 6. in Catalytic Science Series, no. Volume 6, vol. Volume 6. PUBLISHED BY IMPERIAL COLLEGE PRESS AND DISTRIBUTED BY WORLD SCIENTIFIC PUBLISHING CO., 2006. doi: 10.1142/p450.
- [40] G. G. Naples, J. T. Mortimer, A. Scheiner, e J. D. Sweeney, «A spiral nerve cuff electrode for peripheral nerve stimulation», *IEEE Trans. Biomed. Eng.*, vol. 35, fasc. 11, pp. 905–916, nov. 1988, doi: 10.1109/10.8670.
- [41] T. Stieglitz, M. Schuettler, A. Schneider, E. Valderrama, e X. Navarro, «Noninvasive measurement of torque development in the rat foot: measurement setup and results from stimulation of the sciatic nerve with polyimide-based cuff electrodes», *IEEE Trans. Neural Syst. Rehabil. Eng. Publ. IEEE Eng. Med. Biol. Soc.*, vol. 11, pp. 427–37, gen. 2004, doi: 10.1109/TNSRE.2003.819793.
- [42] H. R. Nejad, A. Sadeqi, G. Kiaee, e S. Sonkusale, «Low-cost and cleanroom-free fabrication of microneedles», *Microsyst. Nanoeng.*, vol. 4, fasc. 1, p. 17073, gen. 2018, doi: 10.1038/micronano.2017.73.
- [43] S. Enderling *et al.*, «Sheet Resistance Measurement of Non-Standard Cleanroom Materials Using Suspended Greek Cross Test Structures», *Semicond. Manuf. IEEE Trans. On*, vol. 19, pp. 2–9, mar. 2006, doi: 10.1109/TSM.2005.863248.